Differential Distribution of Functional Co-transmitted Cholinergic and GABAergic Synaptic Inputs onto Substantia Nigra Dopaminergic Neurons

by

Keyrian Louis Le Gratiet

A Thesis Submitted In Partial Fulfillment of the
Requirements for the Degree of
MASTER OF SCIENCE
In the Department of Biology

© Keyrian L. Le Gratiet, 2021
University of Victoria

All rights reserved. This dissertation may not be reproduced in whole or in part, by photocopy or other means, without the permission of the author

Supervisory Committee

Differential Distribution of Functional Co-transmitted Cholinergic and GABAergic Synaptic Inputs onto Substantia Nigra Dopaminergic Neurons

by

Keyrian Louis Le Gratiet

Supervisory Committee

Dr. Raad Nashmi, Department of Biology
Supervisor

Dr. Kerry R. Delaney, Department of Biology
Committee member

Dr. Craig E. Brown, Division of Medical Sciences
Committee member

Abstract

Neuronal communication in the mammalian brain relies on the presynaptic release of neurotransmitters which bind to ligand-gated ion channels found on postsynaptic neurons to modulate neuronal excitability. One such neurotransmitter is acetylcholine (ACh), a small molecule that is the signalling messenger of the cholinergic system. The cholinergic system is involved in a variety of behavioural functions including motor activity, sensory function, and higher executive commands. Dopaminergic neurons in the substantia nigra pars compacta (SNc) and the basal ganglia in general have long been implicated in initiation and completion of voluntary movement. Studies have shown that cholinergic neurons from two brainstem nuclei, the laterodorsal tegmental nucleus and the pedunculopontine nucleus, project onto substantia nigra dopaminergic (DA) neurons in the midbrain and release ACh, GABA or both to modulate motor behaviours. However, with prior research primarily focused on demonstrating the phenomenon of co-transmission itself, the subcellular distribution and dynamics of ACh and GABA release onto SN DA neurons receiving co-transmitted inputs largely remains to be investigated.

The present study investigates the spatial and physiological properties of ACh/GABA co-transmission from brainstem cholinergic axons synapsing onto medial SN DA neurons to understand its role in tuning the neuron's excitatory-inhibitory balance. To that end, we developed a channelrhodopsin (ChR2)-based functional input mapping technique with high spatial resolution to probe the dendritic distribution of ACh and GABA synaptic inputs onto DA neurons in *ChATcre::ChR2* mice. Using this technique, we discovered three different types of monosynaptic inputs from cholinergic axons onto DA cells: co-transmitted ACh/GABA, GABA only, and ACh only. Furthermore, we revealed a somatodendritic patterning of cholinergic input distribution onto DA cells with a predominant GABA conductance along the lateral dendrites and a soma-centered mix ACh/GABA transmission. Physiological findings were corroborated using immunolabeling against VGAT and VAChT, which showed many closely spatially clustered ACh and GABA-specific cholinergic terminals and few truly colocalized VAChT and VGAT terminals. This result revealed that true co-transmission represents a minority of the presynaptic mode of release from cholinergic axons onto medial SN DA neurons, and that the majority actually share closely spatially clustered ACh and GABA-specific cholinergic terminals.

To investigate the dynamic properties of soma-centered ACh/GABA transmission, we restricted our stimulation field to the cell body to measure the contribution of nAChR and GABAR-mediated conductances without recruiting the lateralized population of primary GABA inputs. We then employed a deconvolution method to understand the relative plasticity of contributions of nAChRs and GABARs to ACh/GABA transmission onto DA cells. We confirmed an initial dominant GABAergic component of ACh/GABA transmission that was previously reported. However, we found that the GABAergic contribution had a greater decay compared to the ACh component with repeated stimulations. As such the predominant initial inhibition is followed by a subsequent equalization of excitatory and inhibitory conductances. Finally, we performed similar experiments to compare the short-term plasticity of the isolated GABA conduc-

tance during 15 Hz stimulation between the populations of mix ACh/GABA inputs proximally and the population of primary GABA inputs found on the lateral dendrites 160 μm from the cell body. Interestingly, the lateral GABA component was more sustained across repeated stimulations compared to the proximal GABA conductance, suggesting a differential contribution to excitation/inhibition balance by spatially distributed populations of ACh and GABA inputs from cholinergic axons onto the dendrites of medial SN DA neurons. To our knowledge, this is the first study to examine the distribution and dynamics of ACh/GABA transmission onto midbrain DA system using fine-scale ChR2-assisted subcellular input mapping and conductance deconvolution.

Table of Contents

List of Figures

List of Abbreviations

ACh	Acetylcholine
AIS	Axon initial segment
APV	2-amino-5-phosphonopentanoic acid
Ca_v	Voltage-gated Ca^{2+} channel
C_m	Membrane capacitance
ChR	Channelrhodopsin
ChAT	Choline acetyltransferase
CNS	Central nervous system
CSF	Cerebrospinal fluid
CNQX	Cyanquixaline
DA	Dopaminergic
DHβE	Dihydro-β-erythroidine
E_{Cl}	Chloride reversal potential
E_{cat}	Cationic reversal potential
E/I	Excitation/inhibition
EPSC	Excitatory postsynaptic current
EPSP	Excitatory postsynaptic potential
EYFP	Enhanced yellow fluorescent protein
g_{ACh}	nAChR-mediated conductance
g_{GABA}	GABAR-mediated conductance
GABA	γ-aminobutyric acid
GAD	glutamic acid decarboxylase
HCN	Hyperpolarization-activated cyclic nucleotide-gated
I_A	A-type potassium current
I_{CaL}	L-type calcium current
I_{CaT}	T-type calcium current
I_h	Hyperpolarization-activated cyclic nucleotide-gated current
I_{ToT}	Total current
I-V	Current to voltage
I/O	Input/output
IPSC	Inhibitory postsynaptic current
IPSP	Inhibitory postsynaptic potential
K_v	Voltage-gated K^+ channel
LTD	Laterodorsal tegmental nucleus
nAChR	Nicotinic acetylcholine receptor
MEC	Mecamylamine
MLA	Methyllycaconitine
Na_v	Voltage-gated Na^+ channel

NMDG	N-methyl D-glucamine
PBS	Phosphate-buffered saline
PFA	Paraformaldehyde
PSC	Postsynaptic current
PSP	Postsynaptic potential
R_A	Access resistance
R_i	Internal resistance
R_m	Membrane resistance
sCRACM	Subcellular Channelrhodopsin-2-assisted-circuit mapping
SEM	Standard error of the mean
SD	Standard deviation
SNc	Substantia nigra pars compacta
SNr	Substantia nigra pars reticulata
TH	Tyrosine hydroxylase
TTX	Tetrodotoxin
V	Membrane voltage
V_{hold}	Membrane Voltage potential hold
VAChT	Vesicular acetylcholine transporter
VGAT	Vesicular GABA transporter
VTA	Ventral tegmental area

Acknowledgments

To you dear reader: I would like to thank you for having made it past the list of abbreviations and I wish you a pleasant read throughout this work. Although, let us not kid ourselves, this remains a MSc thesis, and as such, if the act of reading is not mandatory, I would suggest the latest *Nature Reviews Neuroscience* as a more enjoyable source of intellectual satisfaction.

Now that you have been warned*, I will hereby discuss the amazing individuals that I have had the opportunity to become acquainted with at the start of this academic journey.

This work would not have seen the light of day without the combined contributions of my two research mentors, Dr. Raad Nashmi and Dr. Kerry Delaney. I dedicate this thesis to them, and I thank them both for having taken the chance on my 3-year undergraduate self. Their knowledge, support, and advice have made this academic adventure an unforgettable one and I will always be very, very proud to tell people that I have come from their labs. I hope that their teachings can be, in turn and time, shared with the next generation of minds that find joy in the simple act of poking a neuron with a giant glass capillary.

I would like to also thank Dr. Craig Brown, for both his resilience and determination throughout my committee meetings, and for helping me see beyond my understanding to create a more cohesive work.

To Penny, thank you for all your support throughout the years. You rock.

Huge thanks to my friends and *B&B* partners Farnoosh Farhoomand and Laura Hanson for their continued help and camaraderie in the lab and beyond.

Finally, I would like to thank members of the Awatramani and Chow labs for their support and friendship, including but not limited to Santhoosh, Ben, and Alberto.

* If you are one of my Graduate Committee members or my External Reviewer, please feel free to skip the rest of the **Acknowledgements** to proceed directly to the Introduction section below. Thank you for your time and consideration.

Kind regards,

Keyrian.

Chapter 1 – Introduction

1.1 Background and Rationale

Signal transmission in the central nervous system (CNS) relies on the presynaptic release of neurotransmitters which bind to postsynaptic ligand-gated ion channels to modulate neuronal activity. Acetylcholine (ACh), a small molecule comprising one of the oldest neuromodulatory systems across vertebrates and invertebrates (Gerschenfeld; 1973; Bossy et al., 1988; Karczmar, 2007). The cholinergic system is composed of many distributed nuclei of acetylcholine-releasing neurons across the CNS and is responsible for modulating a variety of behavioural functions including motor activity, sensory modulation, and higher executive commands (Miyazawa et al., 2003; Tritto et al., 2004; Drenan et al., 2008, 2010; Guillem et al., 2011; Brown et al., 2012; Leung et al., 2017). Dopaminergic neurons in the substantia nigra pars compacta (SNc) and the basal ganglia in general have long been implicated in initiation and completion of voluntary movement (Andén et al., 1966; Kemp and Powell, 1970; Kandel et al., 2012; Dudman and Gerfen, 2015). This critical role subserved by the SNc is exemplified by the fact that degeneration of the dopaminergic neuronal population in the SNc in Parkinson's patients results in debilitating movement deficits (Steg and Johnels, 1994; Redgrave et al., 2010). Dopaminergic neuronal activity of the SN is modulated by a variety of neurotransmitter systems involving GABAergic, glutamatergic and cholinergic synaptic input (Hammond et al., 1978; Kita and Kitai, 1987; Gerfen et al., 1990; Rinvik and Ottersen, 1993; Futami et al., 1995; Mink et al., 1996; Takakusaki et al., 1996; Lee and Tepper, 2009). Following an increased focus on the investigation of neural circuits responsible for motor control, research has shown that cholinergic neurons from two brainstem nuclei, the laterodorsal tegmental nucleus and the pedunculopontine nucleus, project onto substantia nigra dopaminergic (DA) neurons in the midbrain and releasing ACh, GABA or both to modulate motor behaviours (Estakhr et al., 2017; Li and Spitzer, 2020). The research of Estakhr et al. (2017) was focused on a broad understanding of the long-range connectivity between the dopaminergic and cholinergic nuclei and its behavioral relevance. However, it did not examine how the release of ACh and GABA tunes the physiology of SN DA neurons receiving co-transmitted inputs at a subcellular level along the somatodendritic extent of the neuron. Our current goal is to probe the spatial profile of ACh and GABA release onto SN DA neurons receiving co-transmitted inputs from brainstem cholinergic nuclei, and to investigate at the fundamental level

how the spatial distribution of excitatory and inhibitory inputs onto different somatodendritic compartments of SN DA neurons influences neuronal activity.

1.2 Background Literature

1.2.1 The Substantia Nigra

The Substantia Nigra (SN) is a midbrain nucleus which not only plays a critical role in central sensorimotor processing such as motor learning and execution, but is also involved in reward coding, motivation, and sleep (Haber, 2003; Wise, 2009). The SN modulation of striatal activity (i.e., the nigrostriatal DA system) as part of the basal ganglia motor circuit loop is required for motor control (Dudman and Gerfen, 2015). Damage to either the SN or the nigrostriatal pathway can lead to several neuropathologies such as Parkinson's disease (Fearnley and Lees, 1991; Damier et al., 1999) and Huntington's disease (Albin et al., 1990; Yohrling et al., 2003).

1.2.1.1 Anatomy and Circuitry of the Substantia Nigra

Owing its name to the neuromelanin that accumulates in dopaminergic neurons during cellular aging, the SN is classically divided into two functionally and morphologically distinct regions: (1) the SN pars compacta (SNc) containing dopaminergic (DA) neurons, and (2) the SN pars reticulata (SNr) with inhibitory GABAergic neurons (Zecca et al., 2003; Kandel et al., 2012). While the SNr is primarily involved in the local inhibition of SN DA neuron excitability, the SNc sends long range dopaminergic projections to the striatum, both the putamen and caudate nuclei, and synapses on two separate dopamine-receptive medium spiny neuron subpopulations, the D1 and D2-receptive neuron families (Gerfen et al., 1990; Surmeier et al., 2007; Dudman and Gerfen, 2015; Coddington and Dudman, 2019) in the dorsal striatum. Referred to as the nigrostriatal DA system, dopaminergic modulation of striatal excitability as part of the basal ganglia motor loop differentially affects the output of motor commands. In turn, SN DA neurons receive direct monosynaptic inputs from multiple ascending and descending motor pathways thought to either contribute directly or indirectly to various aspects of voluntary motor functions (Geisler et al., 2007; Donkelaar and ten Donkelaar, 2009; Watabe-Uchida et al., 2012; Kandel et al., 2012). The pathways arise from cortical, subcortical, and midbrain motor structures, including the prefrontal and motor cortices (glutamate), striatum (GABA), reticular formation (serotonergic raphe), the

subthalamic nucleus (glutamate), the superior colliculus (GABA), and the pedunculopontine nucleus (acetylcholine, glutamate, GABA) (Hammond et al., 1978; Kornhuber et al., 1984; Kita and Kitai, 1987; McHaffie et al., 2006; Xiao et al., 2009; Kandel et al., 2012; Estakhr et al., 2017; Galtieri et al., 2017; Gantz et al., 2018) (Fig. 1). Thus, the role of the SN in motor function and goal formation emerges from the reciprocal interconnection of SN DA neurons with nuclei involved in these parallel motor circuits that shape goal-oriented and exploratory behaviours.

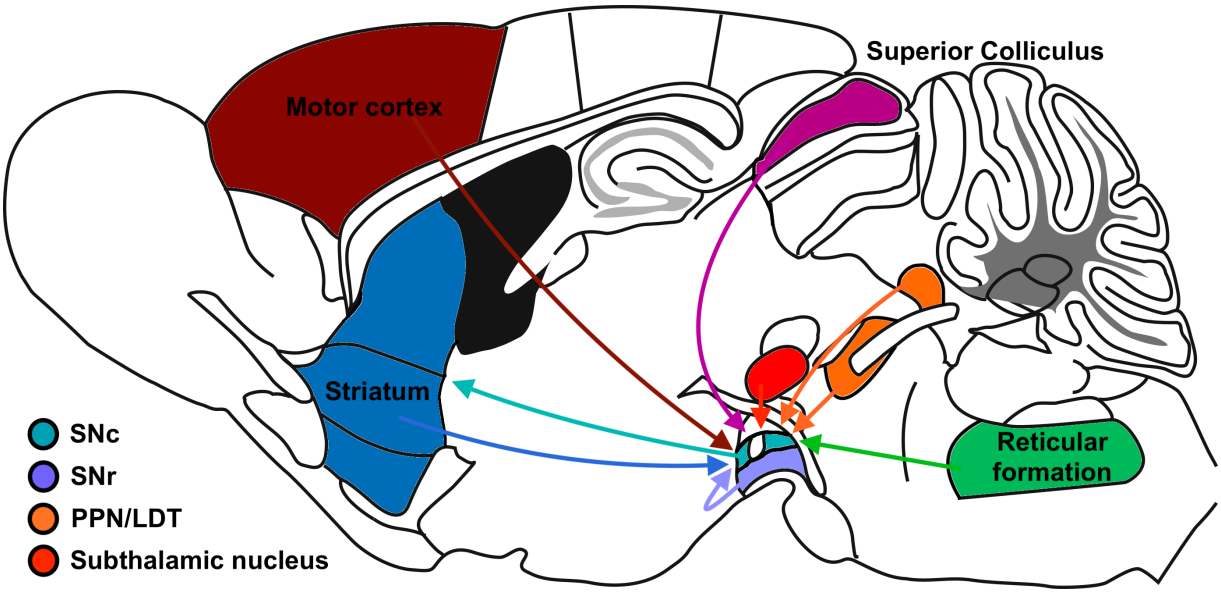

Figure 1. Substantia nigra pars compacta (SNc) dopaminergic neurons integrate inputs from basal ganglia and parallel motor circuits. Anatomical connectivity of SN pars compacta DA neurons relative to nuclei involved in motor circuits. Afferents highlighted are: motor cortex (deep red, glutamate), striatum (blue, GABA), reticular formation (green, serotonin), subthalamic nucleus (red, glutamate), pedunculopontine and laterodorsal tegmental nuclei (orange, acetylcholine, GABA, glutamate), superior colliculus (purple, GABA), and SN pars reticulata (SNr, periwinkle, GABA). SN DA neurons (cyan, dopamine) most directly affect motor circuits by projecting back onto the striatum, the input nucleus of the basal ganglia. Schematic modified from Paxinos and Franklin (2019).

1.2.1.2 Role of the Substantia Nigra in Movement Execution

SN DA neurons exert their largest influence through their interconnectivity with nuclei of the basal ganglia, a highly conserved vertebrate central descending projection circuit (Dudman and Gerfen, 2015). The circuit is primarily involved in action generation whereby intratelencephalic and deep layer pyramidal tract neurons provide motor signals to the dorsoventral striatum as well as the globus pallidus, subthalamic nucleus, and substantia nigra (Kandel et al., 2012). While the basal ganglia output does not directly control spinal motor activity, it monosynaptically and

disynaptically modulates the reticulospinal (reticular formation), rubrospinal (red nucleus), and tectospinal (superior colliculus) pathways that project to motor efferents in the vertebrate spinal cord (Parent et al., 1983; Deniau et al., 2007; Dudman and Gerfen, 2015). A significant portion of basal ganglia output also projects to higher-order thalamic nuclei with effects on cortical activity although its role is still unclear (Anderson and Turner, 1991; Goldberg and Fee, 2012; Phillips et al., 2018; Schwab et al., 2019).

When we consider the overwhelming interconnectivity that SN DA neurons share with projection nuclei involved in all motor pathways, it has been hypothesized that dopaminergic network modulation provides a summary of circuit activity under which a movement was executed. This was recently described as a principle of "cell synchrony" whereby SN DA neurons act as an index of activity across afferent nuclei and signal network consensus in order to facilitate and unify the parallel processing of motor commands (Beeler and Dryer, 2019; Coddington and Dudman, 2019). In this perspective, changes in afferent activity levels would shift the excitation/inhibition balance in midbrain DA neurons that could lead to both ionotropic and metabotropic changes in the excitability of downstream neuronal partners and create sustained effects on behavioral control. This may also explain the symptomatology associated with many basal ganglia disorders that have shown impairment or damage of the nigrostriatal dopamine system such as Parkinson's disease.

1.2.1.3 Substantia Nigra Dopaminergic Neurons: An Overview

Midbrain dopaminergic neurons represent a large heterogenous neural population divided into the substantia nigra pars compacta (dopaminergic cell group A9) and the ventral tegmental area (VTA; dopaminergic cell group A10) (Gantz et al., 2018). The regionalization of those two populations primarily stems from their diverging projection targets with the SN DA system primarily involved in the nigrostriatal pathway while VTA DA neurons project to the nuclei of the limbic system and are thought to play a major role in modulating the affective aspect of reward and motivation (Kandel et al., 2012). However, this still may be an oversimplification as some studies report similar histological patterns of dendritic arborizations between DA neurons of the lateral SN and that of the VTA, suggesting that lateral SN neurons might be an extension of the VTA population (Dudman and Gerfen, 2015; Gantz et al., 2018). Furthermore, recent histological and electrophysiological research have also reported morphological and physiological distinctions

between lateral and medial SN DA neurons, which hints that DA neurons within subregions of the SN could play different roles within their local and long-range networks (Fallon and Loughlin, 1975; Phillipson, 1979; Henny et al., 2012 Evans et al., 2017).

1.2.1.4 Morphological Characteristics of Substantia Nigra Dopaminergic Neurons

SN DA neurons otherwise known as the A9 nucleus are divided into five subregions based on cytoarchitectural and chemical characteristics: the reticular part in the SNr GABAergic region, and the medial, lateral, dorsal, and ventral parts of the SNc (Fu et al., 2012). For instance, DA neurons found in the lateral and medial clusters show marked differences in their calbindin, tyrosine hydroxylase, and GIRK2 channel compositions (Fu et al., 2012). Medial SN DA neurons have a smaller soma diameter and are multipolar while lateral SN DA neurons are commonly bipolar, elongated, and have a larger soma (Fu et al., 2012; Gantz et al., 2018). Differences in morphology and cytoarchitecture between lateral and medial DA neurons in the SN can affect the physiology of those subpopulations when it comes to their respective connectivity patterns with presynaptic partners, which can ultimately shape their integrative properties and thus the behaviour of their local circuits. For example, medial SN DA neurons often project major lateral dendrites in the SNR that shows a high relative density of GAD-positive synapses while dendrites projecting into the SNc and other cartesian planes show equal density between excitatory and inhibitory synapses (Phillipson, 1979; Henny et al., 2012). This heterogeneity in somatodendritic arborizations across the different subpopulations of SN DA neurons could also play a role in the strength and patterning of synaptic connectivity within and between afferent nuclei across the CNS. Recent electrophysiological and immunological evidence from brainstem cholinergic afferents and in particular projections from the pedunculopontine nuclei have suggested diverging patterns of acetylcholine and GABA transmitter release across the lateromedial axial of the SN with lateral SN DA neurons receiving primarily ACh-modulated excitatory inputs while a subpopulation of medial SN DA neurons receive co-transmitted ACh/GABA inputs from cholinergic axons (Estakhr et al., 2017; Li and Spitzer, 2020). Furthermore, while research on the distribution of glutamatergic afferents on SN DA neurons are still sparse, spines and shafts of DA neurons were found to be sensitive to glutamate uncaging, suggesting possibilities of diverging integrative properties of subpopulations of SN DA neurons across multi-synaptic systems (Hage et al., 2016).

One distinguishing feature of midbrain DA neurons is with regards to the location of the axon initial segment (AIS). In many CNS neuron types, the axon emerges from the cell body; however, in midbrain DA neurons, the AIS location is not limited to the soma and the axon is often found on a dendrite, either primary or secondary, at distances as high as 100-140 um away from the cell body (Häusser et al., 1995; Vetter et al., 2001; Moubarak et al., 2019). While a recent study suggests that this morphological variability does not seem to affect the DA neurons' pacemaking output properties, its restriction to a smaller capacitance segment could help in the initiation and conduction of backpropagating action potentials (avoids the voltage sink effect from spike initiation at the soma) and the electrophysiological control of dendritic excitability with regards to the spatiotemporal summation of afferent inputs and the dendritic release of dopamine (Moubarak et al., 2019).

1.2.1.5 Physiological Properties of Substantia Nigra Dopaminergic Neurons

A key feature of SN DA neurons is their autonomous pacemaking and burst firing properties. The physiological phenomena have been reported and studied across various animal models and tissue preparations. Although discrepancies exist with regards to the firing frequency and burst patterns, probably resulting from differences in age, sex, preparations, recording temperatures, etc., SN DA neurons typically fire at low continuous rates (2-4 Hz depending on the external temperature) with transient (~200 ms) increases in activity (Grace and Bunney, 1984a, 1984b; Guzman et al., 2009). The pacemaking activity require the coordination of both high and sub-threshold voltage-gated channels leading to intrinsic temporal changes in ionic conductances across the somatodendritic membrane (Gantz et al., 2018). While the pacemaking cycle is yet to be fully understood, it is suggested to emerge from an interplay between subthreshold Ca currents (I_{CaL},I_{CaT}) from substhreshold voltage-gated Ca channels (Ca_v 1.3, Ca_v 3.x), an hyperpolarization-activated cation current (I_h) mediated by HCN-channels, and a A-type potassium current (K_v 4.3) that activates following AP-mediated hyperpolarization to slow the depolarization induced by I_h and I_{CaL}-I_{CaT} and delay action potential firing (Seutin et al., 2001; Liss et al., 2001; Puopulo et al., 2007; Guzman et al., 2009; Amendola et al., 2012). The pacemaking is thought to maintain extracellular dopamine levels and is critical to the modulation of striatal network activity via the long-range dopaminergic projections (Albin et al., 1989; Gonon and Bloche, 1998; Guzman et al., 2009). It can also ensure a physiological control of the excitation/inhibition (E/I) balance within

the SN itself; indeed, studies have reported that midbrain DA neurons can package and release dopamine from dendritic sites in addition to their long-range axonal target effects, which presupposes auto/paracrine effects in addition to axonal neurotransmission (Wilson et al., 1977; Chen and Rice, 2001; Rice and Patel, 2015). The downstream consequences of dopamine release are mediated by two metabotropic dopamine-sensitive receptors: (1) The D1 receptor subtype, with D1 activation generally increasing membrane depolarization, and (2) the D2 subtype, whose associated secondary signaling mechanism decreases neuronal excitability (Gerfen et al., 1990; Surmeier et al., 2007; Gerfen and Surmeier, 2010). While D1 and D2 receptors subtypes are found on distinct striatal neural populations and are thought to regulate striatal activity within the basal ganglia circuit on sub-second timescale, SN DA neurons also express D2 receptors on their dendrites, which suggest a local autoregulation of dopaminergic pacemaking and might ensure a regionalized basal firing tone across the different subpopulations of SN DA neurons (Beckstead et al., 2004). This could lead to a temporal harmonizing of DA signaling when integrating inputs from afferent nuclei, which further highlights a predominant role of SN DA neurons in encoding network consensus across distributed CNS regions (Coddington and Dudman, 2019).

DA neurons are also electronically compact. In recent studies using Ca imaging, dendritic calcium signals showed no decrement in magnitude throughout the dendritic arbor following somatic current injections (Hage and Khaliq, 2015). Prior research also reported that dendritic-evoked PSPs show little attenuation as a function of distance (Haüsser et al., 1995). Such findings suggest that there is a greater summation potential between temporally overlapping but spatially segregated inputs in SN DA neurons, which can tremendeously increase their integrative capacity of spatially distributed presynaptic inputs. Furthermore, differences in the spatial composition and densities of dendritic voltage-gated channels across the somatodendritic surface have been reported and suggests that SN DA neurons are compartmentalized. The combination of those physiological characteristics with their diversity of synaptic afferent types (glutamatergic, GABAergic, cholinergic) and distinguishing morphologies makes SN DA neurons highly complex.

1.2.2 Cholinergic Neurotransmission in the Mammalian CNS: An Overview

Acetylcholine (ACh) was originally discovered by Dale that noted its physiological actions on tissues in the body (Dale, 1914). Subsequent experiments by Otto Loewi on the frog heart first

demonstrated the actions of ACh as a neurotransmitter: his experiments showed that stimulation of the vagus nerve released "vagusstoff" to slow down the rhythmicity of the heart (Loewi, 1924). Fatt and Katz recorded cholinergic neurotransmission in the frog neuromuscular junction of the skeletal muscle and were the first to determine that the neurotransmitter ACh was released in discrete quanta and to record nicotinic acetylcholine receptor-mediated postsynaptic potentials (Fatt and Katz, 1952). In the mammalian CNS, populations of neurons referred to as cholinergic nuclei have been shown to be involved in motor control, and sensory modulation, as well as to facilitate learning and memory formation. Cholinergic nuclei classically communicate with their postsynaptic partners via release of the small-molecule transmitter ACh that can bind to and activate nAChRs expressed on the cellular membrane of postsynaptic neurons.

1.2.2.1 Nature and Function of Cholinergic Neurons

The cholinergic system is one of the most well-known neuromodulatory systems. Acetylcholine is found in both vertebrates and invertebrates and its effects were first documented in the late 19th century (Schmiedeberg and Koppe, 1869). However, it was not until 1953 that evidence of acetylcholine release was reported in the brain (Eccles et al., 1953). Cholinergic neurons are defined as neurons that produce and release acetylcholine as their main transmitter and are organized in nuclei throughout the CNS. Due to their widespread distribution across brain regions, the role of each individual cholinergic nucleus remains largely unknown. As such, an important part of the research focus on cholinergic transmission has been dedicated to the basal forebrain region that contains six groups of cholinergic neurons that project primarily to the neocortex, with layer 5 being the most densely innervated (Colangelo et al., 2019). Distinct cholinergic nuclei have also been discovered in the brainstem in the latero-dorsal tegmental and pedunculopontine areas, and are thought to be involved in the coordination of eye and limb movements (Matsumara et al., 1997; Okada and Kobayashi, 2015).

1.2.2.2 Cholinergic Transmission in Neural Circuits

A major aspect of neurotransmission involves the kinetics involved with transmitter release. In that regard cholinergic signaling has been initially considered as a “slow” and thus modulatory process, in contrast with glutamatergic transmission which is more commonly perceived as a driver of network activity owing to its fast temporal dynamics (Umbrianco et al.,

1994; Descarries and Meschawar, 2000). The support for this mode of cholinergic neurotransmission, also referred to as volume signaling, was primarily established from anatomical studies reporting the absence of "classical" synapses on cholinergic axons (Muñoz and Rudy, 2014). However, recent developments in ultrastructural techniques and optogenetics have since provided evidence of fast synaptic cholinergic transmission across various CNS regions, including the hippocampus, retina, neocortex, midbrain, that are thought to be critical to various circuit functions and may be complementary to the bulk release mechanism of ACh signaling (Turrini et al., 2001; Kalmbach et al., 2012). This suggests that cholinergic neurons could play a critical modulatory function in their respective circuits at the synaptic and extra-synaptic scale, leading to different temporal modalities of control of neuronal excitability (Sarter et al., 2009; Muñoz and Rudy, 2014)

1.2.2.3 Structure and Expression of CNS Acetylcholine Receptors

Cholinergic nuclei classically communicate with their postsynaptic partners via release of ACh that can bind to and activate an ACh-sensitive receptor expressed on the cellular membrane of postsynaptic neurons. In the mammalian nervous system, ACh receptors are divided into two main types: muscarinic ACh receptors, which are G-protein coupled receptors, and nicotinic ACh receptors (nAChRs), which are ligand-gated cation channels. nAChRs are further subdivided into the muscle nAChR subtype (composed of α, β, γ, δ and ε subunits) and the neuronal nAChR subtype (consisting of α2-α10, β2-β4 subunits) (Nashmi and Lester, 2006; Nashmi et al., 2007). While the muscle form of the nAChR is typically localized at the muscle and is involved in muscle contractions, neuronal nAChRs are found in PNS, CNS and other peripheral tissues (Whiting and Lindstrom, 1986; Whiting et al., 1987).

nAChRs are members of the cys-loop family of pentameric ligand gated ion channels which are characterized by the disulfide bond near their extracellular N-terminus. Each channel is thus formed by assembly of five subunits (Nashmi and Lester, 2006). While α7 subunits can form a fully functional homopentameric receptor, α2-α6 subunits must combine with β2- β4 subunits to form functional pentameric receptors. α8 can form functional homopentameric receptors but are found only in birds, while α9 can form heteropentamers with α10 subunits without any β subunits. Channel activation for neuronal nAChRs occurs following the binding of at least two ACh molecules at the interface of α and β subunits for the heteromeric receptor and at the interface of

the α7 subunits for the homopentameric receptor (Hansen et al., 2005). Upon acetylcholine binding, the nAChR opens and allows a net influx of Na+ and Ca2+, and efflux of K+ that will cause membrane depolarization. Following ligand binding, the receptor only activates for a few milliseconds, while excess ACh is degraded by acetylcholinesterase into choline and acetate and the choline is removed from the synapse by choline transporters. Nicotinic receptor expression is expressed widely throughout the brain with different nicotinic receptor subtypes having different regional and cellular distribution. The most prominent nAChR subtype in the brain, α4β2 (Whiting and Lindstrom, 1986), plays a crucial role in ACh-mediated behavior and is predominantly expressed in both dopaminergic and GABAergic neuron pools in the substantia nigra.

1.2.2.4 Brainstem Cholinergic Modulation of SN Dopaminergic Neurons

DA neurons in the SNc have one of the highest expressions of nAChRs in the brain (Nashmi et al., 2007). Two brainstem nuclei provide the majority of cholinergic inputs to the SNc: the pedunculopontine nucleus (PPN) and the laterodorsal tegmental nucleus (LTD) (Clarke et al., 1987; Cornwall et al., 1990). This simple projection network has gained increased focus due to its involvement in balance and motor coordination in health and disease. DA neurons are strongly excited by nicotine, however, the extent to which the LTD and the PPTN modulate DA activity in the SNc still remains unclear (Nashmi et al., 2007).

The PPN and LTD contain distinct local populations of cholinergic, glutamatergic, and GABAergic neurons with differences in their signaling patterns as well as their projection targets (Xiao et al., 2016; Mena-Segovia and Bolam, 2017; Luquin et al., 2018). Specifically, their cholinergic populations are primarily projecting to the VTA and SN and are involved in the pathophysiology of Parkinson's disease (Perez-Loret and Barrantes, 2016; Mena-Segovia and Bolam, 2017).

Recent electrophysiological, immunological, and behavioural paradigms in mice have revealed differences in transmitter signaling from brainstem cholinergic neurons onto SN DA neurons. In particular, optogenetic activation of brainstem cholinergic terminals in the SNc has revealed a heterogeneous pattern of transmission across the lateromedial axis: (1) Cholinergic axons co-transmit ACh/GABA onto medial SN DA neurons while (2) primarily releasing ACh onto DA neurons from the lateral SN (Estakhr et al., 2017). This antagonistic cholinergic control of SN DA excitability has consequences on motor network activity: light-evoked cholinergic

neurotransmission targeting lateral SN DA neurons was shown to stimulate locomotion while motor inhibition was seen during stimulation of medial SN DA neurons. Furthermore, there is evidence that caudal PPN cholinergic neurons projecting to the SN can switch from ACh to GABA expression following sustained behavioural training in order to improve motor skill learning (Li and Spitzer, 2020). However, it is unclear as to how release of ACh and GABA shapes dendritic integration and tunes the physiology of SN dopaminergic neurons receiving co-transmitted inputs. Based on prior research, a combination of differential spatial and functional characteristics between ACh and GABA release is the most likely phenomenon.

1.2.3 Aspects of Synaptic Integration and Co-transmission in Neural Circuits

1.2.3.1 Somatodendritic Processing in Fast-transmitter systems

The somatodendritic surface area of neurons is covered by a large density of synaptic contacts that allows the cells to receive excitatory and inhibitory inputs, the summation of which being defined by selective changes in the membrane conductances to certain ions across time and space (Wyckoff and Young, 1956; Rasmussen, 1957; Eccles, 1960; Rall, 1962, 1964; Colbert and Johnston, 1996; Stuart et al. 1997). Classically, it is accepted that when the resultant time-dependent change in the membrane voltage across the somatodendritic system exceeds the voltage threshold for voltage-gated sodium channels (Na_vs) to gate open at the region of the axon hillock, it will trigger the firing of sodium action potentials in the postsynaptic neuron (Hodgkin and Huxley, 1952; Bishop 1956, 1958; Rall, 1962). The complex mechanism by which synaptic inputs interact and are processed in the somatodendritic system to either promote or inhibit action potential generation is termed synaptic integration. Initially, synaptic integration was assumed to result from the passive propagation of dendritic inputs to the axon hillock (Bishop, 1956; Rall, 1962). However, experimental evidence now reveals that a lot of the computations done by neurons are compartmentalized to dendrites which possess spatiotemporally distinct active conductances via the selective expression of high- and low-threshold voltage- and ion-gated channels across the dendritic membrane area (Fujita, 1968; Llinàs et al. 1968; Llinàs and Hess, 1976; Wong and Prince, 1978; Wong et al., 1979; Llinàs and Sugimori, 1980; Magee, 1999). These active dendritic conductances tremendously increase the computational power of neurons by introducing channels that, depending on their ionic selectivity and kinetics, can shape postsynaptic

potentials as they propagate in the dendrites. Nevertheless, neuroscience continues to benefit from earlier theories providing elegant mathematical models of dendrites as electrical cables to analyze the integration and spread of excitatory and inhibitory current across the dendritic tree (Fatt and Katz, 1953; Eccles, 1964; Rall, 1958, 1962, 1964).

Complex models analyzing the passive spread of current in dendrites show that the anatomy of dendritic trees plays a predominant role in determining the efficacy of synaptic summation of EPSPs and IPSPs at the axon hillock. In fact, assuming that the membrane capacitance (C_m) and the amplitude of local synaptic conductances remain relatively homogeneous across the dendrites, then dendritic morphology becomes the most important variable shaping the integration of postsynaptic potentials at the axon hillock (Segev and London, 2000; Williams and Stuart, 2002). Compared to local changes in excitatory or inhibitory conductances in proximal dendrites, local changes in excitatory or inhibitory conductances at distal dendritic sites have larger local potential responses due to high input impedance (from the higher membrane resistance R_m compared to that of the soma) and lower membrane capacitance C_m (as distal dendrites tend to have less membrane surface area compared to proximal dendrites) (Agmon-Snir and Segev, 1993; Koch et al., 1996; Jaffe and Carnevale, 1999; Segev and London, 2000; Williams and Stuart, 2002, 2003; Spruston, 2009). Second, more linear summation of EPSPs only occurs with spatiotemporally isolated local changes in excitatory conductances (Fig. 2).

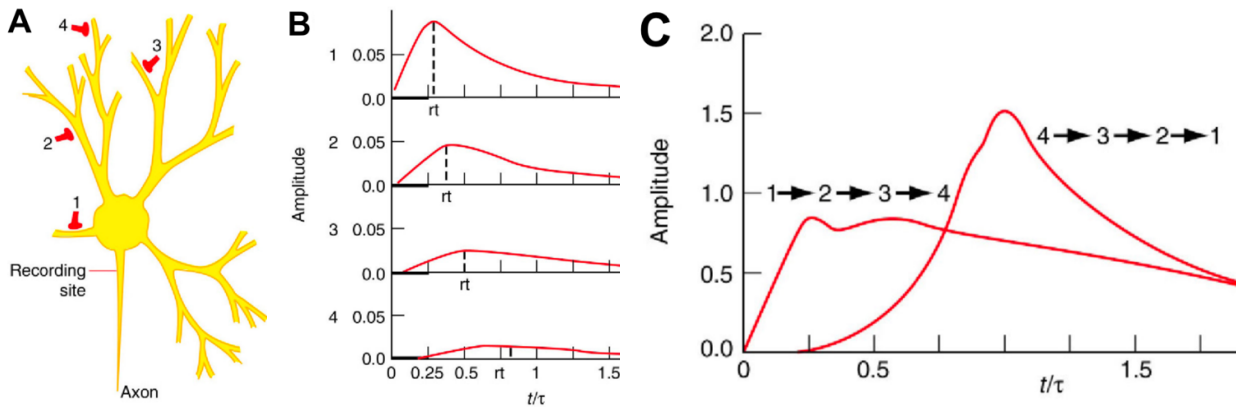

Figure 2. Model of decremental conduction of excitatory postsynaptic potentials (EPSPs) along the dendrites. A. Schematic of a passive model neuron**.** Four excitatory EPSPs (numbered 1 to 4) located at different sites of the dendritic tree are being generated in a sequential manner between t = 0 and t = 0.25 ms and recorded at the axon initial segment. The four EPSPs are assumed to be identical in amplitude and duration at the generation site. **B.** Recorded time-dependent changes in somatic membrane potential for individual EPSPs shown in panel A. It can be observed that due to different dendritic regions being nonequivalent in R_m, R_i, and C_m, EPSPs generated distally in the dendrites while show a longer risetime/decay time and a smaller amplitude as *I* propagates along the dendrites towards the soma and a greater charge leakage with distance) compared to EPSPs generated more proximally to the soma. **C.** Theoretical model of the linear summation of EPSPs discussed in 1.2.3.1. See Hammond (2015) for original figure.

Since the dendritic cross-sectional area reduces distally to the soma, sequential increases in spatially isolated local synaptic conductances result in an asymmetrical somatic response (Fig. 2A; 2B). As shown by Rall (1964), a sequential increase in local synaptic conductances starting from distal locations on the dendritic tree will show a more linear somatic summation than a similar sequential increase in local synaptic conductances that occurs in the opposite direction (from proximal to distal) (Fig. 2C). The framework of this phenomenon of asymmetrical linear summation of EPSPs is derived primarily from the inherent spatial differences in the axial resistance (R_i) and C_m along the dendritic tree (Rall 1964, 1977). First, distal dendritic regions have a higher R_i compared to proximal dendrites (note that $R_i \sim pl/s$, with p being the resistivity, l being the length, and s being the cross-sectional area of the dendrite) due to differences in cross-sectional area while C_m is assumed to be relatively similar across dendritic regions (in reality C_m is slightly smaller at distal dendrites and increases slightly with increasing dendritic diameters, but because C_m is proportional to the lateral surface area of the membrane πrl while R_i is inversely proportional to the cross-sectional area πr^2, variations in cross-sectional area while have much greater effects on R_i than C_m) (Magee, 2000). It follows that for the same synaptic conductance, distal EPSPs will not only show a higher local amplitude due to a higher R_m compared to proximal EPSPS, but a conversely smaller somatic amplitude due to less charge propagation from R_i, charge attenuation from leak channels, and a subsequent increase in capacitance for the same amount of charge propagation from $Q/C_M=V$ (since C_m increases as a function of membrane area in any given dendrite) (Spruston, 2009). Furthermore, distal dendritic EPSPs will show faster local voltage decays compared to proximal EPSPS because proximal dendrites become iso-potential with the soma faster (resulting in less driving force for current flow away from the input site and thus less charge dispersion). Finally, as the current propagates from distal dendrites and charges the membrane over increasing surface areas, distal synapses undergo greater kinetic filtering (from $\tau = R_m * C_m$) compared to proximal synapses. It follows that EPSPs generated distally in the dendrites will show a longer risetime/decay time compared to EPSPs generated proximally when recording voltage potential changes at the soma and will thus be more favorable for summation due to their somatic temporal broadening (Rall 1977; Spruston, 2009).

The simplest model to describe the I/O properties of a neuron consists of passive cable models of dendrites that are segmented into compartmentalized equivalent electrical circuits connected to a soma; however, synaptic input (in the form of a conductance change) and voltage-

gated dendritic currents transform the dendrite in a non-linear computational device. In particular, characteristic dendritic voltage-gated ion channels, such as T-type Ca^{2+}, the HCN, and the A-type K^{+}, have been found in SN DA neurons to actively modulate the shape of synaptic inputs in the subthreshold range and circumvent the inherent limitations of the dendrites' biophysical attributes as passive electronic structures (Gantz et al., 2018). Furthermore, since the I/O characteristics of the neurons are dependent on the summation of excitatory postsynaptic potentials in the subthreshold range, as unitary EPSPs are small when reaching the soma, voltage-gated ion channels that are activated near the resting membrane potentials are likely to have the most profound effect on either facilitating or inhibiting that summation, regardless of its spatiotemporal components.

Such conclusions may lead the reader to think that passive models of dendritic conduction of synaptic inputs have become irrelevant; however, there are issues with that view. First, experimental evidence shows that for some neurons, the summation of EPSPs from distant dendrites do follow Rall's predictions and be linear at the soma (Skydsgaard and Hounsgaard, 1994; Cash and Yuste, 1999). Second, sublinear summation arising from spatiotemporally colocalized synaptic inputs has also been observed and concurs with computational models of passive current spread in dendrites; however, the sublinearity does not necessarily arise exclusively from a decrease in the driving force and membrane resistance, it can also be mediated by active hyperpolarizing dendritic currents such as I_A (Urban and Barrionuevo, 1999). Third, significant spatial averaging takes places in the dendrites: because the spread of local synaptic current is fast and flows rapidly to other dendritic compartments, the electrical characteristics of these not-yet-activated compartments will shape the signal before active dendritic conductances come into play. As such, a research focus on the spatiotemporal consequences of neurotransmitter release on neuronal excitability greatly benefits from accounting for differences in dendritic trees across target neuron populations.

1.2.3.2 Fast Synaptic Signaling via Neurotransmitter Co-release/Co-transmission

During the 20th century debates over the electrical versus chemical nature of neurotransmission, Eccles was the first to formulate what would be later known as Dale's Principle "The same chemical transmitter is released from all of the synaptic terminals of a neurone", when referring to a lecture by Dale in 1935 in which he asked if the nature of peripheral transmitter

release could provide some hint as to the nature of transmitter release at central synapses (Eccles et al., 1954). Initially, it was incorrectly referred to as the one-neuron-one-neurotransmitter hypothesis and as a result, Eccles (1976) proposed that "Dale's principle be defined as stating that at all the axonal branches of a neurone, there was liberation of the same neurotransmitter substance or substances", to encompass the growing body of research reporting co-localization of transmitters in both vertebrates and invertebrates. However, this version of Dale's principle has also been negated (Sossin et al., 1990; Sulzer and Rayport, 2000; Ludwing and Leng, 2006; Takàcs et al., 2018). Indeed, progress in electrophysiological techniques and the recent advent of optogenetics have led to the recognition that some neurons can release multiple fast-acting transmitters, which may or may not be colocalized across release sites (Hnasko and Edwards, 2012; Shabel et al., 2014; Saunders et al., 2015). Examples include starburst amacrine cells that can release acetylcholine and GABA, midbrain dopaminergic neurons that can release glutamate and/or GABA alongside dopamine, and lateral habenula neurons co-releasing glutamate and GABA (Lee et al., 2010; Shabel et al., 2014; Kabanova et al., 2015). Neurotransmitter co-release/co-transmission is a conserved feature with functional relevance. This is supported by changes in relative transmitter levels in specific neuron populations following tissue injury, mental state changes, or behavioral learning (Shabel et al., 2014; Guerriero et al., 2015; McGuire et al., 2019; Li and Spitzer, 2020). Furthermore, it also widens the physiological consequences of local synaptic integration. For example, in the case of co-transmission of two primarily excitatory transmitters, their respective channels can act synergistically or antagonistically at different or similar kinetics, such as the case of the striatal cholinergic interneurons that can release both acetylcholine and glutamate, with differential behavioural outputs (Guzman et al., 2011).

1.2.3.3 Cholinergic Co-transmission in Neural Circuits

The capacity of cholinergic neurons to release multiple neurotransmitters has been the focus of a number of studies and is reported to occur across many brain regions including the basal forebrain, basal ganglia, the pons, the prefrontal cortex as well as the retina (Lee et al., 2010; Shabel et al., 2014; Saunders et al., 2015; Granger et al., 2016; Case et al., 2017; Sethuramanujam et al., 2016; Estakhr et al., 2017; Takàcs et al., 2018; Obermayer et al., 2019). Release of the inhibitory GABA and excitatory ACh neurotransmitter appears to be the principal mode of co-

transmission in cholinergic neurons, although local ACh/Glu co-transmission from striatal cholinergic interneurons has also been suggested (Gras et al., 2008; Guzman et al., 2011).

While the release of two fast-acting excitatory and inhibitory neurotransmitters might be functionally antagonistic, and therefore, seemingly paradoxical, co-transmission of ACh and GABA can create graded physiological effects that finely tune the excitatory-inhibitory balance in downstream neurons. For instance, GABA can locally shunt excitatory ACh inputs on select dendritic sites, which is similar to the mechanism behind motion detection in the mouse retina (Sethuramanujam et al., 2016). GABA and ACh transmission can also act in parallel but with divergent presynaptic release mechanisms whereby one transmitter might have greater amounts released (*i.e.*, facilitates) with continued stimulation of vesicular exocytosis from multiple action potentials while the other transmitter depresses for the same firing regime (Estakhr et al., 2017). Finally, GABA and ACh might be differentially released onto two different dendrites sharing the same synaptic space but with slightly different spatial arrangements leading to divergent diffusional gradients of transmitters in the extracellular space (Svensson et al., 2019).

With prior research primarily focused on demonstrating the phenomenon of co-transmission itself across various nuclei in the CNS, its specific aspects and consequences between target neuron classes largely remain to be investigated. Yet, its prevalence in the cholinergic system hints its fundamental role in modulating goal-oriented motion, attention, and learning.

1.2.4 Research Objective and Hypotheses

1.2.4.1 Research Objective

Our objective is to investigate the spatial and physiological nature of ACh/GABA co-transmission from brainstem cholinergic axons synapsing onto medial SN DA neurons and understand its role in tuning the neuron's excitatory-inhibitory balance. To that end we have developed a fine scale electrophysiological input mapping technique to probe the spatial profile of ACh and GABA release from cholinergic axons onto SN DA neurons at the subcellular level along the somatodendritic extent of the neuron. We hope to uncover how cholinergic axons can locally modulate dopaminergic excitability by mapping the distribution of ACh and GABA release onto the neurons' soma and dendritic arbor.

1.2.4.2 Hypotheses

I will test the hypothesize that ACh and GABA co-transmitted from cholinergic neurons, have different spatial input profiles onto medial SN DA neurons. Differences in spatial release of ACh and GABA could locally tune the excitation-inhibition (E/I) balance in the dendrites and soma of SN DA neurons. I also hypothesize that ACh and GABA release have different activity-dependent dynamics onto SN DA neurons, which, in combination with their spatial distribution, could modulate the neurons' activity.

Chapter 2 – Materials and Methods

2.1 Animal care and breeding

All experiments were conducted in accordance with animal protocols approved by the University of Victoria Animal Care Committee following guidelines for the care and use of animals set by the Canadian Council on Animal Care (CCAC). Mice were housed at the University of Victoria Animal Care Unit (UVic ACU) under a 12 hr light/dark cycle and ad libitum access to food and water. Mouse strains used in this study included *ChATcre::ChR2(H134R)-eYFP*, *ChATcre::ChR2(H134R)-eYFP::Vgat*$^{flox/flox}$, *ChATcre(neodel)::Ai9-tdTomato*, and C57BL/6J.

The *ChATcre::ChR2(H134R)-eYFP* mice were produced from the cross of *ChATcre* mice (Rossi et al., 2011) (JAX stock# 006410), a knock-in mouse strain expressing cre-recombinase driven by the choline acetyltransferase (ChAT) promoter (Lowell et al., 2006), and *ChR2(H134R)-eYFP* mice (JAX stock# 012569), a knock-in mouse strain in which a cre-dependent (*loxP*-flanked stop cassette) channelrhodopsin2 (ChR2) with the H13R mutation and tagged with yellow fluorescent protein (eYFP) inserted in the ROSA26 locus (Madisen et al., 2012) (JAX stock# 012569), was bred to homozygosity for both genes.

To establish the *ChATcre::ChR2(H134R)-eYFP::Vgat*$^{flox/flox}$ mouse line, the *Vgat*$^{flox/flox}$ knock-in mouse strain (Tong et al., 2008) (JAX, stock# 012897) was bred with *ChATcre::ChR2(H134R)-eYFP* mice until homozygosity was reached for all three genes. In this triple transgenic strain, the vesicular GABA transporter (VGAT) gene was deleted via loxP sequences flanking the VGAT exon only in cholinergic neurons expressing cre-recombinase, which also expressed ChR2(H134R)-eYFP.

We also used an *Ai9-tdTomato* (B6.Cg-Gt(ROSA)26Sor$^{tm9(CAG-tdTomato)Hze}$/J) mouse strain (Madisen et al., 2010) (JAX, stock# 007909) that conditionally expresses a red fluorescent protein variant (tdTomato) in Cre recombinase-expressing neurons. Homozygous *ChATcre(neodel)* mice were mated with homozygous *Ai9-tdTomato* mice of the opposite sex to generate a *ChATcre(neodel)::Ai9-tdTomato* reporter line heterozygous for both genes that expresses *tdTomato* in cholinergic neurons (Nazirova et al., 2020). Four to five-week-old offspring (P25-P35) from *ChATcre::ChR2(H134R)-eYFP*-expressing lines were used for electrophysiology and P35 *ChATcre(neodel)::Ai9-tdTomato* mice were used for immunohistochemistry experiments. Separate PCR protocols were performed to confirm the genotypes of the different transgenic mouse strains.

2.2 Brain slice preparation for electrophysiology

Acute brain slices were acquired from P25 to P35-day-old mice of either sex. Mice were deeply anesthetized with isofluorane (Fresenius Kabi, product# CP0406V2) and intracardially perfused with 10 mL of 2-4°C carbogen-bubbled (95% O_2/5% CO_2) N-methyl-D-Glucamine (NMDG) artificial (a) CSF protective cutting solution (92 mM NMDG, 2.5 mM KCL, 1.25 mM NaH_2PO_4, 30 mM $NaHCO_3$, 20 mM HEPES, 25 mM D-glucose, 5 mM Na-ascorbate, 3 mM Na-pyruvate, 0.5 mM $CaCl_2$, and 10 mM $MgCl_2$, pH 7.3). At the end of the perfusion, the mouse was decapitated, and the brain was extracted and immersed in 2-4°C NMDG aCSF for a minute. The brain was then blocked in melted 3% agar-A (CAS# 9002-18-0, Bio Basic Canada) caudal side up and placed on the slicing platform of the vibratome (Leica VT 1000S) with the ventral side facing the blade. The block was immersed in 2-4°C bubbled NMDG aCSF and the brain was sectioned coronally at 320 μm thickness. Sections that included the SNc were subsequently transferred to a pre-warmed (32-34°C) NMDG aCSF solution for an initial protective recovery period of 10 min. After the initial recovery period, slices were washed with room temperature (22-24°C) bubbled recording aCSF (118 mM NaCl, 2.5 mM KCl, 1.25 mM NaH_2PO_4, 24 mM $NaHCO_3$, 12.5 mM D-glucose, 10 mM D-mannitol, 3 mM Na-ascorbate, 1.5 mM Na-pyruvate, 2 mM $CaCl_2$, and 2 mM $MgCl_2$, 308-310 mOsm) before being transferred to a final holding chamber containing room temperature (22-24°C) bubbled recording aCSF for a period of 45 min prior to use for electrophysiology. The recording aCSF solution was made fresh on the day of the experiment and saturated with carbogen to ensure adequate oxygenation and stable pH buffering.

2.3 Electrophysiological recordings

A brain slice was transferred onto the recording chamber and imaged with an upright Nikon FN1 microscope system equipped with a CFI APO 40X W NIR objective (water, 0.8 NA, 3.5 mm working distance). The chamber was continuously perfused with carbogenated recording aCSF and heated to a 31°C with a dual channel temperature controller (cat# TC-344C, Warner Instruments). The medial SNc was identified as the region of the SNc medial to the oculomotor nerve that cut through the SN but lateral to the medial lemniscus as defined previously by our lab (Estakhr et al., 2017). DA neurons in the medial SN were imaged with a Thorlabs Kiralux CMOS camera (CS505MU) under infra-red differential interference contrast (IR-DIC) illumination

microscopy. Whole-cell patch clamp recordings were performed using 4-6 MΩ borosilicate glass electrodes (cat# 1B150F-4, World Precision Instruments) that were filled with one of either two different internal solutions for voltage clamp experiments: (1) an initial K gluconate-based solution was used for the large scale spatial profiling of nicotinic and GABA-mediated postsynaptic currents (PSCs) onto medial SN DA neurons (130 mM K gluconate, 1.3 mM EGTA, 10 mM HEPES, 2 mM $MgCl_2$, 0.5 mM $CaCl_2$, 5 mM phosphocreatine Tris, 3 mM Mg-ATP, 0.2 mM GTP Tris, 2 mM QX314Cl, and 2mM L-glutathione with 80 μM Alexa-555 titrated to pH 7.4, 289 mOsm, E_{Cl} = -80 mV, E_K = -102 mV, Goldman-Hodgkin-Katz theoretically calculated membrane potential (GHK = -70 mV) and (2) a modified Cs gluconate-based solution to optimize the voltage clamp for the fine spatial profiling of nicotinic and GABA-mediated PSCs onto medial SN DA neurons (125 mM Cs gluconate, 2 mM TEABr, 2 mM $MgCl_2$, 10 mM HEPES, 0.5 mM $CaCl_2$, 5 mM EGTA, 5 mM phosphocreatine Tris, 3 mM Mg-ATP, 0.2 mM GTP Tris, 5 mM QX314Br, and 2mM L-glutathione with 80 μM Alexa-555/568 hydrazide titrated to pH 7.4, 295 mOsm, E_{Cl} = -55 mV, GHK = -30 mV). In voltage-clamp experiments cells were held close to their GHK at -60 mV with solution (1) and at -30 mV with solution (2) prior to stepping to various membrane potentials. For accurate measurements, we used cells with holding currents within ±100 pA. For current clamp recordings, the patch pipettes were filled with a K gluconate internal solution (280 mOsm, pH 7.4, E_{Cl} = -65 mV, E_K = -103 mV, GHK = -67 mV) containing: 125 mM K gluconate, 5 mM KCl, 1.3 mM EGTA, 10 mM HEPES, 2 mM $MgCl_2$, 0.5 mM $CaCl_2$, 5 mM phosphocreatine Tris, 3 mM Mg-ATP, 0.2 mM GTP Tris, and 2mM L-glutathione with 80 μM Alexa-555/568 hydrazide (cat# A20501MP/ cat# A10437, ThermoFisher). In all experiments except if otherwise explicitly mentioned CNQX (10 μM) and D-APV (20 μM) were included in the bath to block AMPA/kainate and NMDA receptors, respectively. Nicotinic (DHBE, 1 μM; MLA, 10 nM; MEC, 10 μM) and GABAergic (SR 95531, 10 μM; or Bicuculline, 10 μM) antagonists were added sequentially in co-transmission experiments to confirm the identity of transmitters generating optically evoked EPSCs/IPSCs. For the targeted spatial input mapping experiments, TTX (1 μM) and 4-AP (500 μM) were used to eliminate action potential-dependent release and block K^+ channels necessary for repolarization (Petreanu et al., 2007, 2009; Mao et al., 2011).

All recordings were amplified and low-pass filtered at 4 kHz using a MultiClamp 700B amplifier (Molecular Devices), digitized at a sampling rate of 10-20 kHz with a Digidata 1440A A/D board (Molecular Devices), and recorded using pCLAMP 10.2 acquisition software

(Molecular devices). The holding voltage in voltage clamp was corrected for the liquid junction potential (-13 mV) and the series resistance was corrected 40%. In current clamp mode, bridge balance and capacitance neutralization were applied. Cells with access resistance R_A found between 10 to 20 MΩ were kept for analysis while cells with R_A > 25 MΩ or with an ΔR_A greater than 20% over the course of the recording session were excluded. Electrophysiological responses were analyzed in Igor Pro 8 (Wavemetrics, Lake Oswego, OR, USA) using the Neuromatic plugin (version # 3.0, http://www.neuromatic.thinkrandom.com).

DA cell phenotype was confirmed by measuring hyperpolarization-activated cyclic nucleotide gated currents (I_h) in SN neurons in cells recorded with K gluconate based internal solution and by also performing post-hoc immunohistochemistry against tyrosine hydroxylase in brain slices containing dye-filled SN neurons that showed responses of interest, as described (Estakhr et al., 2017). SN DA neurons were readily distinguished by their large I_h currents compared to GABAergic neurons as well as by their colocalization of the Alexa 555/568 dye with the TH antibody (Fig. 3 and Fig. S1).

2.4 LED light stimulation and imaging

Brain slice physiology was done with ultrafast collimated LEDs mounted on a microscope for illumination through a CFI APO 40X W NIR objective (water, 0.8 NA, 3.5 mm working distance), with peak wavelengths at 365 nm, 470 nm, and 565 nm (Thorlabs, M365LP1, M470L3-C5, M565L3). We restricted the emission of LED spectra to prevent the cross-stimulation of channelrhodopsin, Alexa dyes, and caged glutamate compounds with the following bandpass filters (Semrock, Thorlabs): 365 nm LED with a 376 nm long-pass dichroic filter, 470 nm LED with a 473 ± 23 nm filter, and 565 nm LED with a 562 ± 20 nm filter. Light power was controlled through LED drivers (Thorlabs LEDD1B or custom made) using analog voltage pulses. The voltage pulse intensity was adjusted to obtain the desired illumination density as measured with a photometer (PM100USB, Thorlabs). Photon fluxes were set to 40 mW/mm^2 at 365 nm, 20 mW/mm^2 at 470 nm, and 5 mW/mm^2 at 565nm. The LED illumination duration and onset were recorded with a photodiode system integrated into the light path and the signal was directed to the Digidata 1440A A/D converter. The field of illumination was manually controlled with a pinhole that allowed projections of circular light spots with diameters ranging from 30 to 560 nm. Pinhole

settings had been calibrated prior to the experiments with different objectives using a stage micrometer and appropriate fluorescent slides.

Photocurrents measurements were single trial and access resistance R_A was monitored throughout. Either a single, three, or five sweeps were taken per trial depending on the experiment. All experiments included at 30-second period in the dark between sweeps to allow for opsin and/or caged compound recovery.

Expression of ChR2(H134R)-eYFP was confirmed by brief visual inspection of the oculomotor nerve and surrounding fluorescence levels in the SN region with the 470 nm LED (Thorlabs). For spatial mapping experiments, dye-filled dopaminergic neurons were imaged between recording trials with Nikon CFI APO 40X W NIR objective (water, 0.8 NA, 3.5 mm working distance) using Thorlabs Kiralux CS505MU under identical illumination parameters throughout: 565 nm LED (Thorlabs) at 5 mW/mm^2 with the 562 ± 20 nm filter.

2.4.1 LED light optogenetic stimulation for coarse spatial mapping of ACh and GABA currents

To generate the conductance maps in **Figure 3**, light-evoked synaptic currents were recorded at the pharmacologically defined E_{Cl} (V_{hold} = -80 mV) and E_{Cat} (V_{hold} = 0 mV) under bath application of AMPA and NMDA receptor inhibitors (CNQX, D-APV) at each optical stimulation coordinate to voltage-isolate the individual ACh and GABA currents. Stimulation coordinates were manually recorded during electrophysiological recordings. The peak of light-evoked ACh and GABA currents at each coordinate was computed offline with peaks at or below noise level (5 pA) assigned a value of 0. Peak values (pA) for ACh and GABA PSCs were subsequently divided by their driving force (Δ80 mV) to derive the respective ACh and GABA-mediated conductance (nS). Conductance values and their assigned spatial coordinates were organized into XYZ triplets in Igor Pro 8 to generate a Delauney triangulation of the data and create the conductance maps via XYZ contouring. Contouring levels (n = 11) were automatically assigned and the interpolation was set as linear in light of the resolution of optical stimulation (circular beam diameter, 275 μm).

2.4.2 LED light optogenetic stimulation for synaptically localized spatial mapping of ACh and GABA currents

To generate the fine-scale inputs maps in **Figure 4**, light-evoked synaptic currents were recorded at -55 mV and 0 mV to voltage-isolate ACh and GABA PSCs, respectively, under bath

application of AMPA and NMDA receptor inhibitors (CNQX, D-APV). The stimulation field was reduced to a 30 μm-diameter area and recordings were made in the presence of TTX and 4-AP to eliminate action potential-dependent release and evoke voltage-isolated ACh and GABA monosynaptics by limiting excitation at the presynaptic terminals (Petreanu et al., 2007). The presence of ACh or GABA inputs for each individual stimulation field was verified by repeated light-stimulation (3 pulses, 5 Hz) and the input nature of each field was assigned based on PSC repeatability (*i.e.,* the local inputs were assigned as ACh or GABA or mix ACh/GABA if at least 2 out of 3 PSCs were above noise level, 5 pA, at each voltage potential hold). Stimuli were restricted to fluorescently labeled dendrites and delivered sequentially following manual re-focusing to cover the entire dendritic field of sampled neurons. Stimulation coordinates were manually recorded during electrophysiological recordings and inputs maps were aligned onto the reconstructed DA neurons post-physiology. Peak conductance values were calculated based on the peak current measurement of the first pulse for each local field divided by their respective nAChR (E_{cat}=0, Δ55mV for mix ACh/GABA fields or Δ70mV for primary ACh fields) and GABAR driving forces (~Δ55mV, which approximates the driving force in light of theoretical E_{Cl} = -55 mV and experimental E_{Cl} = -58 mV).

2.5 Immunohistochemistry

Mice were deeply anesthetized via isofluorane (Fresenius Kabi, product# CP0406V2). Once unresponsive, the were intracardially perfused with PBS, followed by paraformaldehyde via a peristaltic pump (Masterflex Easy Load, Cole-Parmer, cat#EW-07518-00) at a rate of 6 mL/min. All solutions were prepared one day prior to the intracardial perfusion and left at 4°C overnight. The perfusion began with 25 mL of PBS (pH 7.6), followed by 25 mL of 4% paraformaldehyde (PFA) (in PBS, pH 7.6, Electron Microscopy Sciences, cat#15710), and finally 20 mL of PBS (pH 7.6) in order to flush residual PFA and to reduce autofluorescence of the tissue. At the end of the perfusion, the mouse was decapitated, and the brain was extracted and put into a 4% PFA solution (in PBS, pH 7.6). After two days in the dark and kept at a constant temperature of 4°C, the brain was removed from solution and a razor blade was used to remove the cerebellum. The brain was then placed rostral side up in a weight-boat and submerged in 1.5% Agar A (Bio Basic, cat#4583) and left to harden for 15 min before slicing. 80 μm thick coronal sections were

cut using a vibratome (Pelco 101, 1000 Series) and put onto lysine-coated slides (NewSilane, Newcomer Supply, cat# 5070, or Superfrost® Plus Gold, Fisher Scientific, cat# 15-188-48).

Brain sections on slides were washed three times with PBS (pH 7.6) for 10 min and then permeabilized with 0.25% Triton X100 for 10 min. The sections were washed again three times for 10 min with PBS and successively blocked with 10% donkey serum (diluted in PBS; Jackson ImmunoResearch, cat# 017-000-121) for 30 min. The primary antibody (tyrosine hydroxylase, abcam, cat# AB76442, host: chicken; vesicular ACh transporter (VAChT), Millipore, cat# ABN100, host: goat; vesicular GABA transporter (VGAT), Millipore, cat#AB5062P, host: rabbit) was diluted in 3% donkey serum (diluted in PBS) at 1:250 and incubated at room temperature overnight. Sections were washed with PBS three times for 10 min. The secondary antibody (Alexa Fluor 405 IgG secondary antibody, Invitrogen, cat# A-31556; Alexa Fluor 488 IgG secondary antibody; Alexa Fluor 647 IgG secondary antibody, Invitrogen, cat# A-21447; Cy3-conjugated IgG secondary antibody, Jackson ImmunoResearch Labs, cat# 711-165-152) was diluted in 3% donkey serum, at 1:300 concentration and incubated overnight at room temperature. Brain sections were then washed with PBS three times for 10 min. Finally, sections were washed three times for 3 hours and mounted with 80 µL Immunomount (Immu-MountTM, Thermo Scientific, cat# 9990402). Following coverslipping, slides were left at 4°C overnight before imaging.

For cell type confirmation and cellular reconstruction of recorded DA neurons filled with Alexa-555/568 hydrazide dye, brain slices were fixed in 4% paraformaldehyde (pH 7.6, diluted in PBS) for one hour on a shaker and stored at 4°C overnight prior to immunolabeling. The labeling protocol followed that described by Kàradòttir and Attwell (2006). For dopaminergic neuron labeling or axonal identification, slices were incubated overnight on a shaker at room temperature with either a primary antibody against tyrosine hydroxylase (Millipore, cat# AB1542(CH), host: sheep) or with a primary antibody against ankyrin G (Invitrogen, cat# 33-8800, host: mouse) diluted in 3% donkey serum (diluted in PBS) at 1:250. Secondary antibodies (Cy3-conjugated IgG secondary antibody, Jackson ImmunoResearch Labs, cat# 711-165-152; Alexa Fluor 647 IgG secondary antibody, cat# A-31571) were diluted in 3% donkey serum, at 1:300 concentration and incubated overnight on shaker at room temperature. Finally, sections were washed three times for 3 hours and mounted with 100 µL Immunomount (Immu-MountTM, Thermo Scientific, cat# 9990402). Following coverslipping, slides were left at 4°C overnight before imaging.

2.6 Confocal Microscopy

Images were acquired using a Nikon C1si spectral confocal microscope. For neuronal reconstruction and AnkyrinG imaging, sections were imaged with a 40X air Plan Fluor DIC objective (0.75 NA, 0.66 mm working distance) and a 60X oil-immersed Plan Apo VC objective (1.4 NA, 0.12 mm working distance), respectively. For neuronal reconstruction, Alexa fluor 555 and 568 hydrazide were excited using a 561 nm laser line at 10-25% maximum transmission of a Melles Griot laser while Alexa Fluor 647 was excited using a 640 nm laser line at 1% maximum transmission of a 100 mW Obis laser. Images were collected at 5.52 µs pixel dwell time and averaged over 3 scans through a 60 µm diameter pinhole with a spectral detector gain set at 220. Settings were optimized to ensure that greyscale intensity values fell below saturating value (<4095 for 12-bit greyscale) and kept consistent across all images and experiments. I collected ~200x200 µm2 z-stack images with a 0.5 µm step size over a ~20-30 µm depth across a spectral range of 660-750 nm (A647), or 570-590/670/730 nm (A555/A568). Neuronal reconstruction was performed in Fiji (ImageJ, version 2.1.0/1.53c) with the Simple Neurite Tracer (SNT) plugin installed (https://imagej.net/SNT). For the vesicular transporter immunostaining experiments, sections were imaged with a 40X oil-immersed Plan Apo VC objective (1.3 NA, 0.24 mm working distance). Alexa Fluor 647 was excited using a 640 nm laser line at 1% maximum transmission of a 100 mW Obis laser, tdTomato was excited using a 561 nm laser line at 8% maximum transmission of a Melles Griot laser, Alexa Fluor 488 was excited using a 488 nm laser line at 2% maximum transmission of a 40 mW Argon laser, and Alexa CF 430 was excited using a 405 nm laser line at 3.2% maximum transmission of a Melles Griot diode laser. Images were collected at 5.52 µs pixel dwell time and averaged over 2 scans through a 60 µm diameter pinhole with a spectral detector gain set at 220 (A647, tdTomato, CF430) or 175 (A488). Settings were optimized to ensure that greyscale intensity values fell below saturating value (<4095 for 12-bit greyscale) and kept consistent across all images and experiments. I collected 150x150 µm2 z-stack images with a 0.5 µm step size over a ~20 µm depth across a spectral range of 660-750 nm (A647), 580-640 nm (tdTomato), 493-543 nm (A488), and 430-480 nm (CF430).

2.7 Analysis of Confocal Microscopy Images

Analysis of vesicular transporters in cholinergic axons using confocal microscopy images was performed in Fiji (ImageJ, version 2.1.0/1.53c) with the 3D imageJ suite installed

(https://imagej.net/3D_ImageJ_Suite). A 4.0-pixel median filter was applied to all images of the stacks followed by subsequent background subtraction (rolling ball radius: 50.0 pixels). Automated thresholding with the RenyiEntropy method was applied to VAChT and VGAT sub-stacks that successfully selected puncta while maximally excluding noise. Similarly, automated thresholding with the Triangle method was applied to ChAT and TH sub-stacks that successfully selected axons and dendrites, respectively. Corresponding thresholded VAChT and VGAT slices were combined with thresholded ChAT slices using the Image calculator command with an "AND" operator to analyze only co-localized VAChT-ChAT and VGAT-ChAT puncta. For the lateral stacks, to restrict VAChT-ChAT and VGAT-ChAT puncta analysis to the vicinity of TH dendrites, co-localized VAChT-ChAT and VGAT-ChAT slices were combined with thresholded TH slices that had been 3D dilated by 1µm (maximum 3D filter application on thresholded TH slices, x = 7 pixels, y = 7 pixels, z = 3.5 pixels). Puncta analyses were performed using the 3D Object Counter plugin (voxel limit: 10/500) and the 3D distances plugin (from the 3D ImageJ suite) with parameters set for closest neighbor computation and border distances.

2.8 Algebraic deconvolution of nAChR and GABAR conductances

Light-evoked ACh/GABA currents were recorded at membrane potentials between ~-70 to ~+10 mV stepped in 10 mV increments under repeated stimulation (15 Hz, 6 pulses). The average current response was measured over a time window (10 ms following current onset) to increase signal-to-noise ratio. Responses were consequently modeled as the sum of their respective nAChR- and GABAR-mediated currents (least-squares fit) as per Manookin et al. (2010):

$$I_{TOT}(V) = W_{GABA} * g_{GABA} * (V\text{-}E_{Cl}) + W_{ACh} * g_{ACh} * (V\text{-}E_{cat}),$$

where $I_{TOT}(V)$ is the total current at the membrane voltage V, E_{Cl} the chloride reversal = -58 mV, and E_{cat} the cationic reversal = 0 mV. g_{GABA} and g_{ACh} are the respective basis conductance functions of GABARs and nAChRs, respectively, normalized to 1 at -60 mV (see below). W_{GABA} and W_{ACh} denote the conductance weight at -60 mV and represented the reported values for GABA and ACh conductances.

Based on previous experiments (Manookin et al., 2010), the basis function for GABA (g_{GABA}) was defined as an exponential equation:

$$g_{GABA}(V) = b + \exp^{a*V}$$

where a = 0.00543 and b = 0.278 are constant experimentally derived from the fit of light-evoked GABAR I-V relationships measured from DA cells (5 cells from 5 mice, Fig. 6) under pharmacological inhibition of nAChRs and AMPA/NMDARs. g_{GABA} was finally multiplied by a factor to normalize the conductance at -60mV to 1 (*i.e.,* multiplying by the inverse of g_{GABA} at -60mV): 1.046.

The basis ACh function was well described by a simplification of the Woodhull equation (Haghighi and Cooper, 1998) to account for the voltage-dependent inward rectification of nAChRs:

$$g_{ACh}(V) = 1/(1+a/\exp^{b*V})$$

where a = 23.1 and b = -0.0615 are constants experimentally derived from the fit of light-evoked nAChR I-V relationships measured from DA cells (3 cells from 3 mice, Fig. 6) under pharmacological inhibition of GABARs and AMPA/NMDARs. g_{ACh} was consequently multiplied by a factor to normalize the conductance at -60 mV to 1 (*i.e.,* multiplying by the inverse of g_{ACh} at -60 mV): 1.576.

2.9 Statistical Analyses

Values are reported as mean ± standard error of the mean (SEM) and were computed using R (v4.0.3, 2020). Data were graphed using Igor Pro software. When applicable, assumptions of normality and equal variances were tested using a Shapiro-Wilk normality test and a *F*-test, respectively. Nonparametric F2-LD-F2 or F1-LD-F1 factorial tests (Brunner et al., 2002) followed by post-hoc paired Wilcoxon rank sum tests with continuity correction were used to evaluate longitudinal data when parametric assumptions were not met. A Linear regression mixed model (Type III ANOVA with Satterthwaite's method) followed by post-hoc pairwise contrast tests for main effects with Tukey correction was used when parametric assumptions were not met for 2-factorial non-longitudinal data. Wilcoxon rank-sum tests were used to evaluate mean group differences when parametric assumptions were not met. If both samples had normal distribution but unequal variances, a Welch's t-test was used to examine differences between the two means. Statistical significance was determined at the alpha level of 0.05 in all analyses.

Chapter 3 – ACh and GABA Inputs from Cholinergic Axons show a Differential Spatial Profile onto the Dendrites of SN DA Neurons

3.1 Introduction

Since the seminal computational work of Wilfrid Rall (1962) and major experimental studies in the late nineties to early 2000s, it has become clear that dendritic morphology critically influences neuronal excitability by differentially filtering local time-dependent changes in excitatory and inhibitory currents (Rall, 1958, 1964, 1977; Bekkers and Stevens, 1996; Stuart and Spruston, 1998; Gentet et al., 2000; Roth and Haüsser, 2001). Consequently, an appreciation of network functionality requires an understanding of the synaptic properties between defined neuron populations and knowledge of the precise location of synaptic inputs on the neuronal membrane since those synaptic inputs spatiotemporally summate with intrinsic neuronal events to shape the neurons' input-output properties, which ultimately defines the activity of the neuronal network (Stuart et al., 2016). Initial approaches to study synapse distribution on the dendrites of CNS neurons have typically used fluorescence or EM microscopic techniques which, being mainly performed on fixed tissue, cannot probe the functional significance of synaptic inputs with regards to their location on the neurons' dendrites (Stuart et al., 2016). Furthermore, the anatomical overlap of axonal projections with dendritic branches as a classical predictor of input strength and/or connectivity between different neuronal populations has not been corroborated in recent experiments (Callaway, 2002; Callaway and Yuste., 2002; White, 2002; Petreanu et al., 2009; Mao et al., 2011). Therefore, since an understanding of network characteristics requires an accurate physiological probing of circuit connectivity, there has been a call for research to implement a functional approach to investigate spatial profiles of synaptic inputs between target nuclei and understand how such profiles shape the multi-synaptic integrative properties of neurons and define their firing patterns. This becomes all the more critical in systems involving neurotransmitter co-release/co-transmission, which adds another layer of integrative complexity (Lee et al., 2010; Shabel et al., 2014; Saunders et al., 2016; Granger et al., 2016; Case et al., 2017; Estakhr et al., 2017; Takàcs et al., 2018; Obermayer et al., 2019).

Paired whole-cell recordings have long been developed to probe CNS neural networks and detect functional synapses; however, those methods often rely on fully preserved pre- and post-synaptic neuron populations and are thus mainly limited to local circuits (Luo et al., 2008). Neurotransmitter uncaging has also been used for that purpose. However, the spillover effect

produced by the uncaging can cloud local input contributions (Schubert et al., 2001; Anastasiades et al., 2018). With the discovery of the light-activated cation channel Channelrhodopsin-2 (Chr2) from the algae *Chlamydomonas reinhaardtii* (Nagel et al., 2003) and its successful viral re-engineering to drive its expression in target neurons, optogenetics has become a common methodology to selectively photostimulate presynaptic axonal fibers and measure the evoked excitatory/inhibitory postsynaptic responses in downstream neurons of interest (Boyden et al., 2005; Li et al., 2005; Nagel et al., 2005; Lin et al., 2011). It has also permitted a development of fine scale optical stimulation techniques used to investigate neuronal circuits by probing the functional connectivity between target nuclei without requiring the preservation of the cell body of the presynaptic neurons nor defined axonal tracts as it can effectively photostimulate individual axons even when severed from their somata (Wang et al., 2007; Petreanu et al., 2007). Subcellular ChR2-assisted-circuit mapping was one such technique developed to systematically probe the functional connectivity between target nuclei over long range projections (Petreanu et al., 2007, 2009). The study of Petreanu and colleagues was the first of its kind to effectively map out monosynaptic connections between neurons using optical stimulation. Since then, many studies have used optogenetics to map neuronal connectivity in the mammalian brain (Wang et al., 2007; Petreanu et al., 2009; Mao et al., 2011; D'Souza et al., 2019; Bhatia et al., 2019). Moreover, the selective expression of ChR2 in target populations provides better presynaptic specificity while avoiding some of the pitfalls of earlier methodologies. However, current optical circuit maps have caveats: (1) many studies performing subcellular input mapping focused on the effects of local inputs on the neuron's membrane potential and thus did not supress the large dendritic Na, K, and Ca conductances from voltage-gated channels, resulting in significant electrotonic filtering as a function of distance from the soma and thus presenting a "somatocentric view" of dendritic input distribution (Petreanu et al., 2009; Dembrow et al., 2015); (2) The optical stimulation protocol was derived from methods in fluorescence microscopy and the grid of photostimuli has been presented in a raster pattern, which limits a targeted optical following of the dendritic tree for fine scale photostimulation; (3) Grid-based photostimulation necessitates a lower objective lens to cover a larger field of view, resulting in a stimulation resolution of ~60 μm, which is very large in comparison to the diameter of most somatas and dendrites (Petreanu et al., 2007, 2009; Mao et al., 2011; D'Souza et al., 2019). Here, we have developed a fine-scale ChR2-based input mapping technique that permits a true optical following of the dendritic tree with fine resolution (~10 μm)

while minimizing electrotonic filtering and we have used it to probe the spatial profile of ACh and GABA release onto medial SN DA neurons receiving co-transmitted inputs from cholinergic brainstem nuclei, and to investigate how the spatial distribution of excitatory and inhibitory inputs from cholinergic axons shapes the physiology of those SN DA neurons.

3.2 Results

3.2.1 Functional ACh and GABA Release from Cholinergic Axons onto Mouse SN Dopaminergic Neurons Receiving Co-transmitted Inputs Show a Differential Spatial Profile

Prior studies have shown that cholinergic neurons from select brainstem nuclei project onto VTA and SN DA neurons in the midbrain and can release ACh and GABA in a co-transmitted manner and modulate motor behaviours (Estakhr et al., 2017; Li and Spitzer, 2020). To assess the nature and physiological consequences of this co-transmission of excitatory and inhibitory neurotransmitters onto DA neurons in the medial SN, we combined local optogenetic stimulation of cholinergic axons with whole-cell patch clamp recordings of DA neurons in *ex-vivo* brain slices from *ChATcre::ChR2(H134R)-eYFP* mice. *ChATcre::ChR2(H134R)-eYFP* mice express Cre recombinase under the transcriptional control of the *ChAT* promoter, enabling selective expression of the opsins in cholinergic neurons (Lowell et al., 2006; Estakhr et al., 2017). The medial SN region is separated from the VTA by the dorsal medial lemniscus and the lateral SN by the tracts of the oculomotor nerve (Fig. 3A). Whole-cell patch clamped DA neurons were identified by their large I_h currents and the identification was confirmed via post-hoc immunolabeling (Fig. 3A; Fig. S1A-B). Experiments were done on DA cells showing ACh/GABA co-transmission. Photostimulations of cholinergic axons were performed in voltage clamp mode across a range of stepped membrane potentials to enable the simultaneous recording of synaptic ACh and GABA currents (Fig. 3B). Individual components were pharmacologically isolated using either a cocktail of nAChR antagonists (methyllycaconitine [MLA], and mecamylamine [MEC]) or a GABAAR antagonist (gabazine) to confirm that components displayed identical latencies and thus were co-transmitted (Fig. 3C). We first investigated the spatial profiles of ACh and GABA release onto DA neurons displaying full-field light-evoked ACh/GABA co-transmitted postsynaptic currents (PSCs) to assess whether the distribution of co-transmission was similar across the dendritic arbor (Fig. 3D1-3). Interestingly, we found a differential spatial profile of ACh versus GABA

transmission whereby the ACh conductance was primarily found to extend from the soma ventrodorsally while the GABA conductance was found to be more uniformly distributed, albeit with a stronger conductance gradient in the lateromedial axis (Fig. 3E1-2; Fig. S1C-E). We also investigated the excitatory-inhibitory balance between ACh and GABA and found a net excitation gradient in the dorsal direction, which highlighted the differential spatial profile of ACh and GABA release from cholinergic fibers onto DA neurons receiving co-transmitted inputs (Fig. 3F).

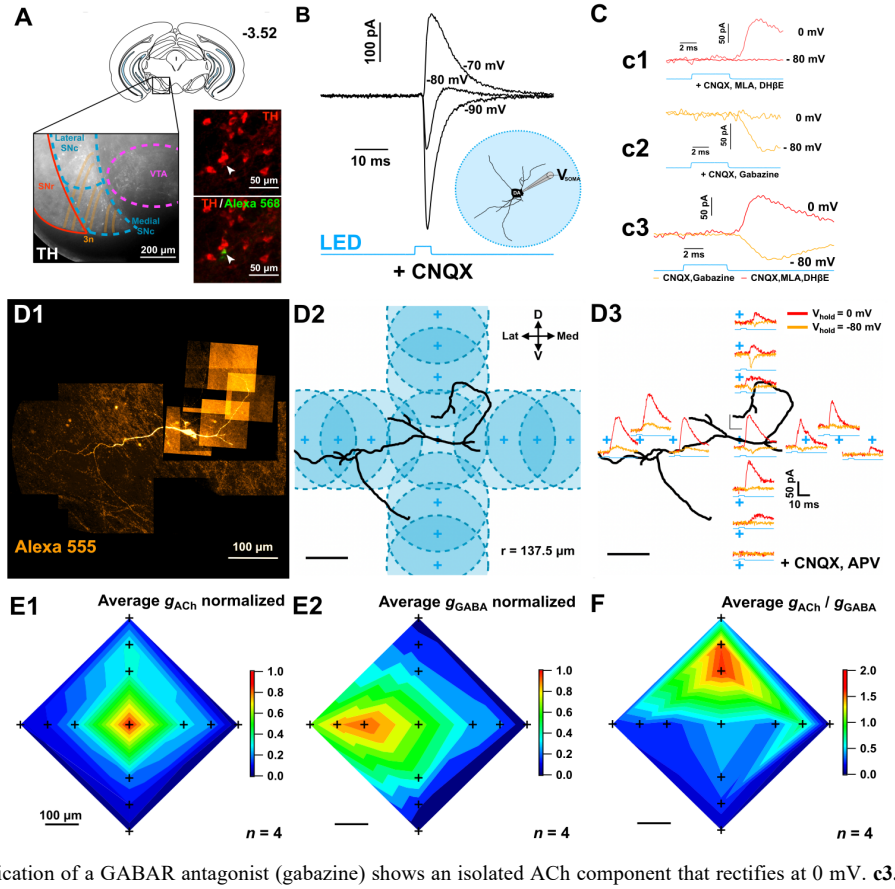

Figure 3. Medial SN DA neurons receiving ACh/GABA PSCs show differential distributions of ACh/GABA conductances. A. Diagram of a coronal slice (Bregma -3.52 mm) showing the medial substantia nigra region where we studied ChAT-DA connections using optogenetic stimulation of ChAT::ChR2 axons and whole-cell recordings of DA neurons. The oculomotor nerve (3n) was used as a landmark to target the medial SN. Patched neurons were dye-filled for post-hoc TH immunolabeling to confirm DA phenotype. **B.** Whole-cell recordings in voltage-clamp mode of full-field light-evoked ChAT-DA transmission at different voltage potentials under bath application of the AMPAR antagonist CNQX (10 µM). **C.** Drugs confirm the identity of the light-evoked PSCs from cholinergic fibers onto a medial SN DA neuron. **c1.** Bath application of CNQX and nAChRs antagonists (DhβE, 10 µM, and MLA, 100 nM) onto a medial SN DA cell receiving putative light-evoked co-transmitted ACh/GABA PSCs isolates a GABA component that reverses at -80 mV. **c2.** Washout of nAChR antagonists and bath application of a GABAR antagonist (gabazine) shows an isolated ACh component that rectifies at 0 mV. **c3.** Superimposition of pharmacologically isolated GABA (**c1**) and ACh (**c2**) PSCs corroborates co-transmission. **D1.** Example medial SN DA neuron showing light-evoked, co-transmitted ACh/GABA PSCs from ChR2+ cholinergic axons under full field 470 nm LED stimulation (field diameter: 550 µm). Alexa 555 hydrazide (40 µM) was included in the patch pipette for imaging during electrophysiological recordings and neuronal reconstruction. **D2.** Experimental design to investigate the distribution of ACh/GABA conductance across the DA dendritic fields. Upon determining that the DA cell received co-transmitted ACh/GABA PSCs under full field LED stimulation, the stimulation field was reduced (radius =137.5 µm) and moved in four orthogonal vectors to locally sample ACh and GABA-mediated PSCs in the DA neuron. Each vector covered a range of 320 µm from the origin point set on the cell body of the neuron. Three zones per vector were sampled with an initial distance step of 160 µm from the origin, and two subsequent steps of 80 µm (see 1, 2, and 3 on the panel) to cover the full mapping range. **D3.** Light-evoked, voltage-isolated ACh (orange) and GABA (red) PSCs for each stimulation area sampled onto the medial SN DA neuron as per the design outlined in (D2). **E1-2, F.** Spatial mapping of voltage-isolated light-evoked ACh (recorded at -80 mV) and GABA (recorded at 0 mV) conductances for medial SN DA cells. *n* = 4 cells from 4 mice.

We developed a fine-scale ChR2-based input mapping strategy to understand the nature of ChAT-DA transmission and measure the strength of inputs from cholinergic axons onto medial

SN DA neurons across their dendritic arbor. For all subsequent experiments, the patch pipette contained a cesium gluconate-based internal solution with bromide forms of QX314 and TEA to block Na^{2+}, K^{+}, and Ca^{2+} channels and improve the quality of the voltage clamp at depolarized potentials while preserving membrane properties (Zhang et al., 1994; Talbot and Sayer, 1996; Kaczorowski et al., 2007). It reduced the electrotonic filtering experienced by other methodologies but shifted the effective chloride reversal to less depolarized potentials (Bormann et al., 1987; Petreanu et al., 2007). Whole-cell voltage clamp recordings confirmed the voltage shift of the biphasic component of ACh/GABA co-transmission, which was verified by pharmacology (Fig. 4A; Fig. S2A). The stimulation field was subsequently reduced to a 30 μm-diameter area and recordings were made in the presence of TTX and 4-AP to eliminate action potential-dependent release and evoke voltage-isolated ACh and GABA monosynaptics by preventing initiation of action potential propagation along axons of passage but limiting excitation at the presynaptic terminals (Petreanu et al., 2009). Under these conditions, brief 470 nm LED pulses (5ms) depolarized ChR2-expressing presynaptic boutons, triggering the local release of ACh and GABA (Fig. 4B; Fig. S2B1-3). Stimuli were restricted to fluorescently labeled dendrites and delivered sequentially following manual re-focusing to cover the entire dendritic field of sampled neurons. Measurements of the point spread function indicated that our methodology maps specific types of inputs with higher subcellular spatial resolution (9.8±3.5 μm) than previous techniques and can suggest axonal directionality of inputs (Fig. S3A-E). Aligning the input maps with the reconstructed DA neurons post-physiology revealed the dendritic locations of synaptic contacts with ChR2-positive cholinergic axons (Fig. 4C). Furthermore, voltage-clamping at -55 and 0 mV while locally stimulating the individual 30 μm fields revealed three different types of monosynaptic transmitter release from cholinergic axons: co-transmitted ACh/GABA, primary GABA, and primary ACh (Fig. 4D1-3). The distribution of inputs was sparse across the DA dendrites, suggesting a restricted number of synaptic contacts (Fig. 4E1-6). However, the alignment of all input maps revealed a somatodendritic patterning of input distribution consistent with the predominant GABA conductance laterally and soma-centered ACh/GABA transmission, irrespective of the location of the axon initial segment (Fig. 4E1-6 and 2G; Fig. S2C1-5). All cells showed both ACh/GABA and primary GABA input types and most cells showed all three (Fig. 4F). Superimposition of all reconstructed cells with their conductance maps suggested that ACh/GABA inputs were found close the cell body while primary GABA and ACh inputs extended

towards the lateral and dorsoventral axis, respectively (Fig. 4I1-2). Furthermore, we observed a positive excitation to inhibition gradient in the mediodorsal axis that corroborated with the coarse spatial data (Fig. 4J). Finally, we found a higher GABA conductance for the mixed ACh/GABA inputs compared to other input types but a greater density of primary GABA inputs overall (Fig. 4K). This suggests that there might be a difference in either the density of synaptic contacts between cholinergic axons and medial SN DA neurons as a function of the neurotransmitter released, or a different probability of release, or both (Estakhr et al., 2017; Li and Spitzer, 2020).

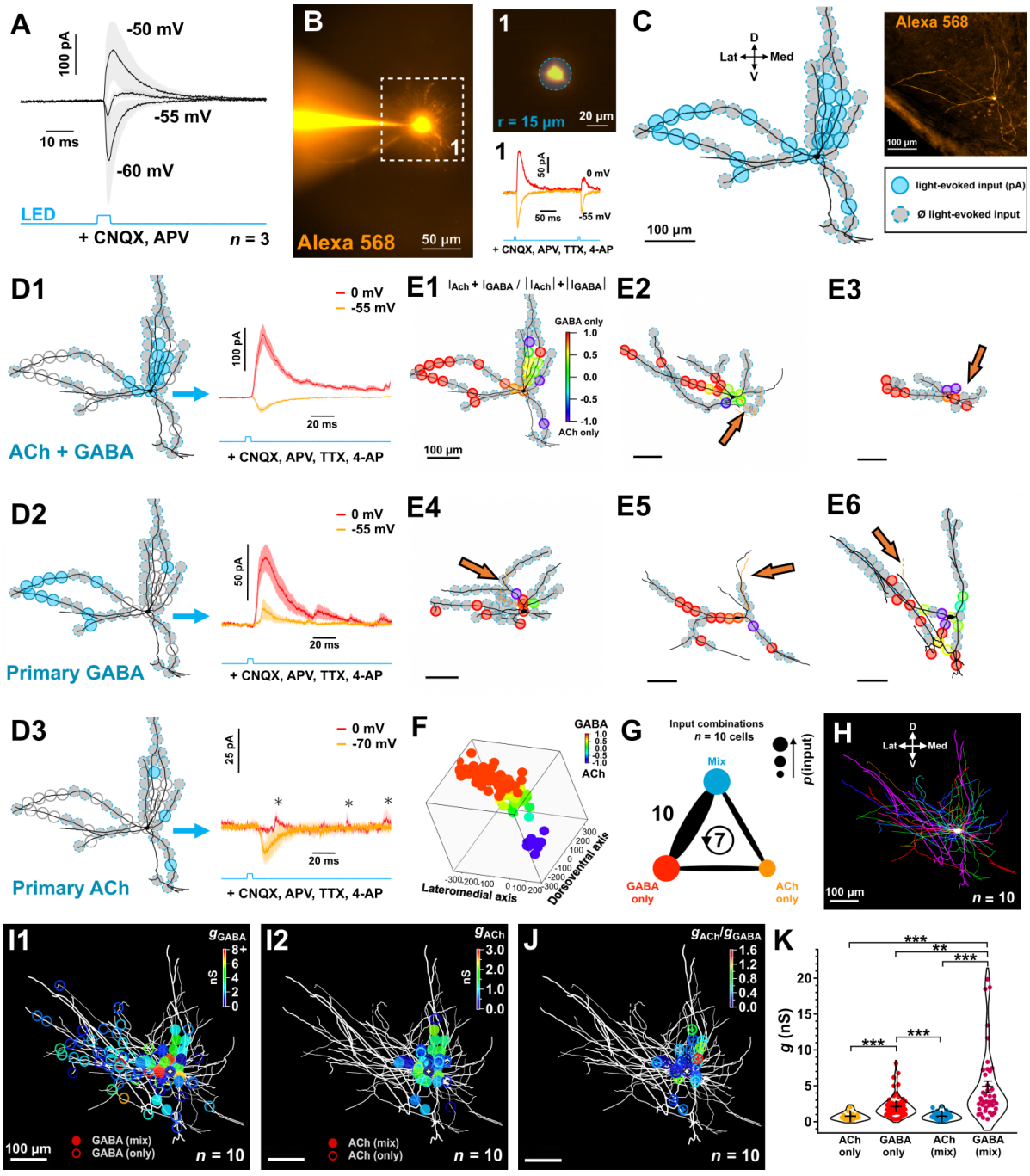

Figure 4. Three types of cholinergic monosynaptics differentially distribute onto the dendritic field of DA neurons. A. Whole-cell voltage-clamp recordings of light-evoked ChAT-DA transmission at different holding potentials in the presence of CNQX and D-AP5 (n = 3 cells from 3 mice). Note the biphasic component indicating putative ACh/GABA co-transmission. **B.** Example of monosynaptic light-evoked ACh (hold = -55 mV) and GABA (hold = 0 mV) PSCs from a 30 µm field stimulation on a medial SN DA neuron dye-filled with Alexa 568 (80 µM) following bath application of CNQX (10 µM), D-AP5 (20 µM), TTX (1 µM), 4-AP (500 µM). **C.** Input map overlaid on the recorded neuron following post-hoc neuronal tracing. Inputs where PSCs were evoked are color-coded. Recorded neurons in this and subsequent experiments were orthogonally aligned to the midline position. **D.** Whole-cell recordings of monosynaptic light-evoked PSCs show a differential subcellular distribution of ACh and GABA release from ChAT::ChR2 axons. PSCs were organized by input type (mean ± SEM is plotted). Asterix indicates spontaneous IPSCs. **E1-6.** Examples of inputs maps overlaid on reconstructed neurons. Relative contribution of ACh and GABA to the total recorded current across the two voltage potentials (-55 and 0 mV) is color-coded from each local stimulation field. AnkyrinG staining on DA cells (n = 5 from 5 mice) prior to neuronal tracing reveals variation in distance of

the axon initial segment from soma (orange arrows). **F.** 3D superimposition of input maps as a function of the relative contribution of ACh and GABA to each input shows a distribution of input types across orthogonal axes. **G.** Summary of input type pairs observed on mapped DA neurons. Thickness of the connecting line indicates the frequency with which a pair was observed. Values are number of cells per pair. The circular arrow represents cells where all three input types were observed. **H.** Superimposition of mapped DA neurons orthogonally aligned to the midline and cell-body centered. Note the asymmetry of dendritic fields. **I1-2**. ACh and GABA input maps aligned on superimposed neurons. ACh and GABA conductances were derived for individual local inputs and organized by input type. White arrow marker shows soma location. **J.** Absolute ratios of ACh and GABA conductances for mix ACh/GABA inputs. Orthogonal mapping reveals a mediodorsal gradient of excitation. For **E-J**, n = 10 cells from 10 mice. **K.** ACh and GABA conductances per input as a function of the input type. Statistical significance $*p < 0.05$, $**p < 0.01$, $***p < 0.001$ was assessed by Aligned Rank Transformed (ART) ANOVA with post-hoc pairwise contrast tests for main effects with Tukey correction. Data are shown as mean ± SEM.

3.2.2 Anatomical Evidence Showing a Differential Subcellular Localization of ACh and GABA Presynaptic Release Sites Along the Somatodendritic Extent of SN DA Neurons

Prior studies have identified that SN DA neurons are innervated by long-range cholinergic projections from the dorsolateral tegmental and pedunculopontine nuclei (Xiao et al., 2016; Estakhr et al., 2017; Li and Spitzer, 2020). Furthermore, research suggested that subpopulations of cholinergic neurons in those nuclei, in particular the PPN, possess the cellular machinery for acetylcholine and GABA transmitter release in their presynaptic terminals found in the SN. To further validate the differential nature of synaptic release from cholinergic axons onto medial SN DA neurons, we used *ChATcre(neo-del)*$^{+/-}$*::Ai9-tdTomato*$^{+/-}$ mice that show selective labeling of cholinergic neurons and their axonal processes (Nasirova et al., 2020). Triple labeling the SN for TH, VAChT, and VGAT, identified proportional differences in the number of VAChT and VGAT puncta found in tdTomato+ putative cholinergic terminals as a function of the DA somatic or lateral dendritic regions (Fig. 5 A-B). Similar to Estakhr et al. (2017), we identified VAChT-VGAT puncta that were either fully co-localized or within ≤ 1μm distance (both criteria we referred to as "mix" VAChT/VGAT puncta); however, mix puncta represented the minority of putative presynaptic cholinergic terminals in contrast with individual VGAT+ only and VAChT+ only puncta in identified tdTomato+ axons (Fig. 3B-C; Fig S2D1-4). Expanding on the findings by Li and Spitzer (2020) and consistent with our electrophysiological results, a much greater proportion of VGAT+ puncta (69%) were found within a 1 μm vicinity of the TH+ dendrites 300 μm lateral to the soma of medial SN DA neurons while similar amounts of VGAT+ (49%) and VAChT+ (40%) puncta were found in proximity of the cell bodies (Fig. 5C). Meanwhile, the lower absolute number of lateralized puncta is likely reflective of the lower density of lateral TH+ dendrites 200-400 μm away from the somata of medial SN DA cells (Fig. 5D-E). Finally, differences in VGAT+ and VAChT+ puncta sizes in identified tdTomato+ putative terminals

suggest a greater density of GABA transmitter packaging across cholinergic terminals compared to ACh packaging, which in addition to differences in release probabilities outlined in Estakhr et al. (2017), further strengthens the differences in ACh and GABA conductances observed with soma-centered ACh/GABA transmission (Fig. 5F).

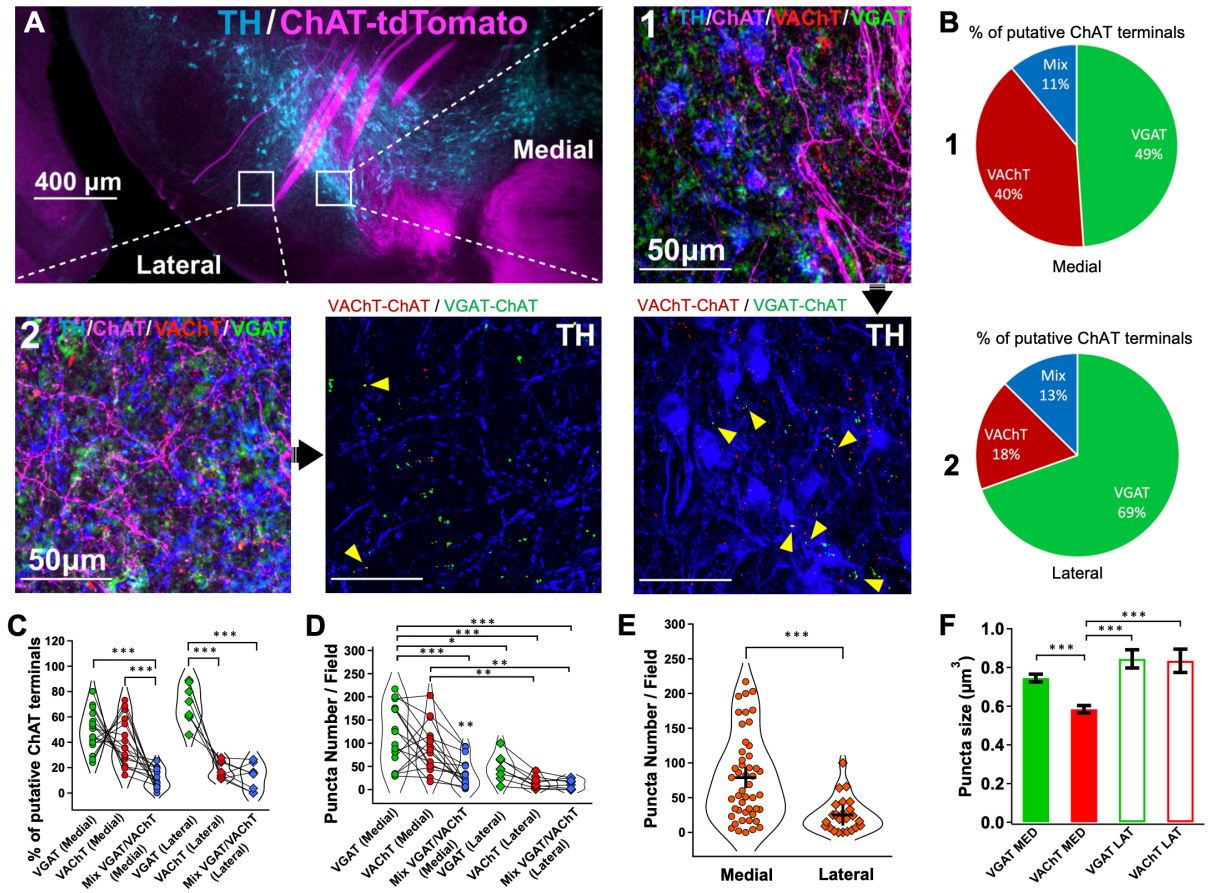

Figure 5. Differential subcellular localization of ACh and GABA presynaptic release sites along the somatodendritic extent of SN DA neurons. A. Experimental design to identify the distribution of vesicular transporter expression of cholinergic axons in the SN. *ChATcre(neo-del)*$^{+/-}$*::tdTomato*$^{+/-}$ mice were used to visualize the cholinergic innervation of the SN. Coronal sections containing the SN were triple labeled for TH, VGAT, and VAChT. Two locations were bilaterally sampled (2 z-stack images centered on the cell bodies of medial DA neurons, one lateral z-stack image) to enable a comparison in transporter expression for putative cholinergic terminals between the somatic and lateral dendritic regions of DA cells. Analyses were performed on VAChT+:tdTomato+ and VGAT+:tdTomato+ puncta. For the lateral field, puncta at distances ≥ 1 µm away from TH+ dendrites were excluded from analysis. Yellow arrows indicate co-localized puncta. $n = 4$ mice, $n = 6$ z-stack images per mouse. **B.** Summary of the percentage of VAChT+ and VGAT+ terminals in cholinergic axons projecting to either the somata of DA cells or in the vicinity of lateralized TH+ dendrites. **C.** Percentage of VAChT+, VGAT+, and mixed VGAT+:VGAT+ (≤ 1µm away) in putative cholinergic terminals in the SN as a function of their location. **D.** VAChT+, VGAT+, and mixed VGAT+:VGAT+ puncta numbers in putative cholinergic terminals in the SN as a function of their location. For **C-D** Linear regression mixed model (Type III ANOVA with Satterthwaite's method) followed by post-hoc pairwise contrast tests for main effects with Tukey correction. **E.** Absolute number of puncta in putative cholinergic terminals in the SN as a function of their location. Two-sided Welch's *t*-test. **F.** VAChT+:tdTomato+ and VGAT+:tdTomato+ puncta sizes as a function of their location. Linear regression model followed by post-hoc pairwise contrast tests for main effects with Tukey correction. For **C-F**, $n = 4$ mice, $n = 6$ z-stack images per mouse. Each dot represents one z-stack. $n = 24$ z-stacks per group (VGAT+, VAChT+, VGAT+:VAChT+). $n = 48$ medial z-stacks, $n = 24$ lateral z-stacks. *$p < 0.05$, **$p < 0.01$, ***$p < 0.001$. Data are shown as mean ± SEM.

Chapter 4 – GABA and Nicotinic Acetylcholine Receptor-mediated Conductances Reveal Spatially-Defined Differential Short-Term Plasticities

4.1 Introduction

Prior studies have revealed ACh/GABA transmission onto medial SN DA neurons via long-range innervation of the SN by subpopulations of brainstem cholinergic neurons that co-express the cellular machinery for ACh and GABA synthesis, packaging, and release (Estakhr et al., 2017; Li and Spitzer., 2020). However, since the focus of the research was on the modulatory role of cholinergic neurons within the scope of DA-mediated motor function, the extent of ACh/GABA co-transmission was not quantified, and little is known about its functional implications on cellular DA excitability. While our prior chapter explored the diversity and patterning of ACh and GABA transmission across the dendritic arbor of medial SN DA neurons, this current chapter will be focused on our efforts to investigate its physiological characteristics.

Recent optogenetic experiments have shown a dichotomy in the plasticity of ACh and GABA release following activation of cholinergic terminals that are due to differences in release probabilities with low stimulation frequencies (5 Hz) supporting inhibition while high stimulation frequencies (15 Hz) would suggest a shift towards excitation (Estakhr et al., 2017). However, this cellular mechanism did not account for the diversity of distribution of ACh and GABA inputs and the higher proportion of distinct ACh- and GABA-containing cholinergic terminals compared to co-localized terminals. Furthermore, electrophysiological data did not fully correlate with the associated shift in the excitability of medial SN DA neurons at physiological pacemaking potentials. To investigate aspects of soma-centered ACh and GABA transmission, we restricted our stimulation field to 80 μm focused on the cell body in order to measure the contribution of ACh/GABA transmission without recruiting the lateralized population of primary GABA inputs. We then employed a deconvolution method developed by Manookin et al. (2010) whereby I-V plots obtained following repeated optogenetic stimulation can be decomposed into the weighted sum of their individual GABAR and nAChR conductances. The deconvolution model provides great advantages for understanding the physiological nature of ACh versus GABA transmission in that it can estimate their respective receptor contributions without pharmacological application of

drugs that could disturb the local network properties and thus make it challenging to draw any valid assumptions (Manookin et al., 2010; Sethuramanujam et al., 2016).

4.2 Results

4.2.1 Generating the nAChR and GABAR Basis Functions

We first measured the full-field isolated voltage-dependent properties of nAChRs and GABARs using a cocktail of receptor antagonists across several medial SN DA cells (n=8 cells, 8 mice) to ensure a high fidelity of deconvolution. Cholinergic synaptic currents were evoked under bath application of glutamate and GABA receptor antagonists (CNQX + D-APV + bicuculline) and showed an inward rectification with a cationic reversal (E_{cat}) at 0 mV (Haghighi and Cooper, 1998) that was well described by a derivation of the Woodhull equation (Fig. 6A1-2). Similarly, pharmacologically isolated GABAR-mediated currents showed a slight outward rectification with a chloride reversal (E_{Cl}) at -58 mV, and the current-voltage behaviour was fit by a single exponential function as previously described (Manookin et al., 2010; Fig. 6B1-2).

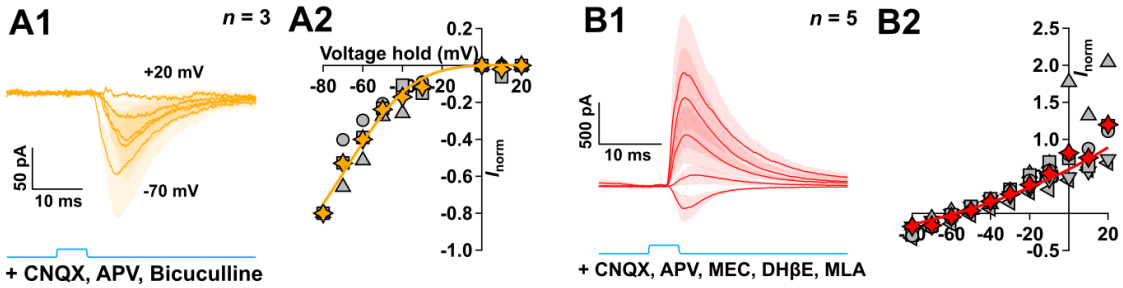

Figure 6. Generating the nAChR and GABAR basis functions. A1. Whole-cell voltage-clamp recordings in DA neurons of light-evoked nAChR currents measured from -80 to +20 mV in 10 mV increments (-70,-50,-30,-10, +20 mV are plotted) in the presence of CNQX, D-APV, and bicuculline. *n* = 3 cells from 3 mice, mean ± sem is plotted. **A2.** The normalized I-V relationship computed from the nAChR current averaged over a 10 ms period from time to onset. Each grey marker represents an individual cell, average is plotted by the yellow marker. The average I-V was fit by a derivation of the Woodhull equation (see **Methods**). **B1-2.** Similar to (A1-2), GABAR currents were measured following pharmacological isolation (CNQX, 10 µM; D-APV, 20 µM; MEC, 20 µM DHBE, 10 µM; MLA, 100 nM) and the I-V relationship was fit by an exponential function. *n* = 5 cells from 5 mice, mean ± SEM is plotted.

4.2.2 nAChRs and GABARs Show Differential Conductance Dynamics in ACh/GABA Transmission

To estimate the relative contributions of the different receptors to the total current response with repeated local stimulations on the cell body, PSCs were evoked over a range of holding

potentials (Fig. 7A). The mix I-V relationship was then modeled as a weighted linear sum of the basis functions for nAChRs and GABARs, which upon deconvolution, yielded an estimate of the fractional conductance for each receptor type at -60 mV (Fig. 7B). A dominant GABAergic component in the initial stimulation was consistently observed across five cells (g_{GABA} = 72.2 ± 5.5 %, g_{ACh} = 27.8 ± 3.9 %; where g_{GABA} and g_{ACh} indicate the respective GABA and nACh receptor conductances; Fig. 7C). However, the weight of the GABAergic contribution showed a greater decay compared to the ACh component with repeated stimulations, suggesting an initial inhibition followed by a subsequent equalization of excitatory and inhibitory conductances (Fig. 7D-E). To validate the analysis from the deconvolution model, we tested its performance under bath application of nAChR antagonists: in this case, the ACh-mediated inward current component seen at hyperpolarized holding voltages and the associated nAChR conductance was suppressed to levels that were not significantly greater that zero (Fig. S4A-C).

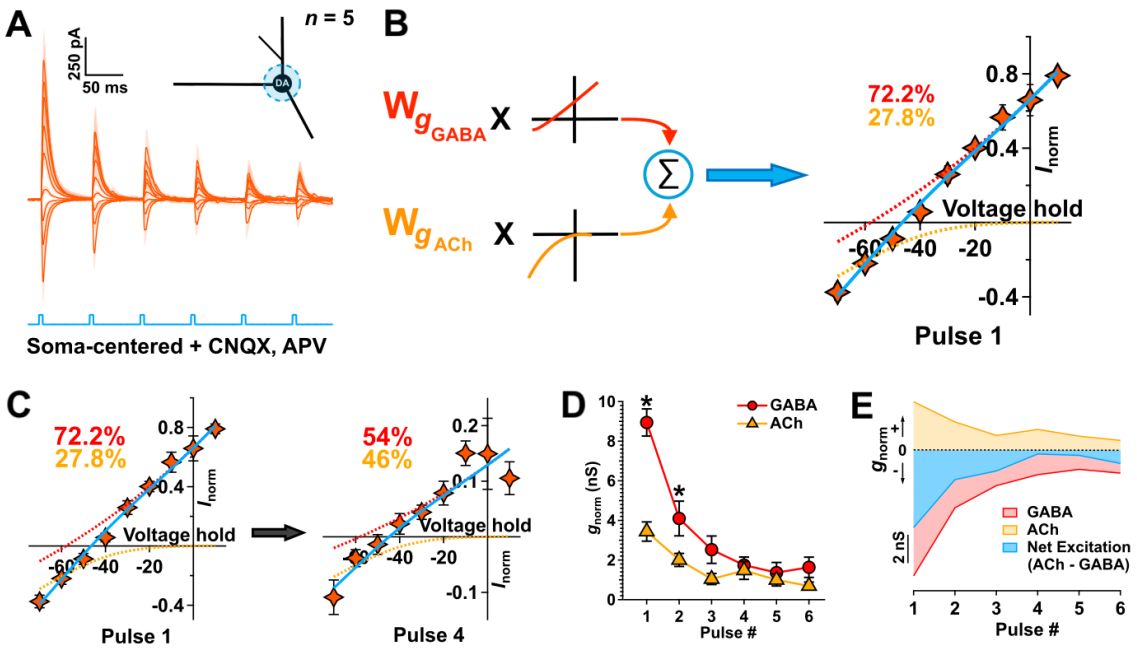

Figure 7. nAChRs and GABARs show different conductance dynamics with repeated ACh/GABA transmission. A. Whole-cell voltage-clamp recordings of local (80 µm) soma-centered mix nAChR- and GABAR-mediated currents with repeated ChR2 stimulation (6 pulses, 15 Hz) over a range of holding potentials (-70 to 10 mV, 10 mV increments). Responses are measured in the presence of CNQX and D-APV. *n* = 5 cells from 5 mice, mean ± SEM is plotted. **B.** The I-V relationship computed from the current in (A) averaged over a 10 ms period from time to onset. The average current was modeled by a weighted linear sum of the basis fit functions of each receptor type as estimated in Fig. 6 (solid blue line, see **Methods**). The computed fractional conductances (g_{ACh},g_{GABA}) at -60 mV were obtained following deconvolution (see text) and are indicated on the graph for the first ChR2 pulse. Responses were initially dominated by GABARs (dashed red line). **C.** The average I-V relationship between the first and fourth pulse. The estimated GABAR contribution (dashed red line) decreases with repeated stimulation to levels equal to that of the nAChR component of the response (dashed orange line). **D.** Normalized estimated ACh and GABA conductances as a function of the pulse number. Nonparametric F2-LD-F2 factorial test followed by post-hoc paired

Wilcoxon rank sum tests. **E.** Temporal evolution of nAChR (orange) and GABAR (red) conductances estimated at -60 mV in the same DA neurons using deconvolution. Subtracting the GABA from the nAChR conductance yields an estimate of the net excitation/inhibition (blue). For **A-E**, $n = 5$ cells from 5 mice. *$p < 0.05$, **$p < 0.01$, ***$p < 0.001$. Data are shown as mean ± SEM.

4.2.3 The Isolated GABAR Conductance Is More Sustained Laterally

Following the robust performance of the deconvolution procedure, we performed similar experiments to investigate the plasticity of the isolated GABA conductance between the populations of mix ACh/GABA inputs proximally and the population of primary GABA inputs found on the lateral dendrites 160 μm away from the cell body (Fig. 8A-C). The I-V relationships between distal and proximal GABA inputs were overlapping on the first pulse across the range of voltage potentials, suggesting that the voltage clamp data did not suffer from space-clamp issues and were of adequate quality for the deconvolution procedure (Fig. 8D). Interestingly, the lateral GABA component was more sustained across repeated stimulations compared to the proximal GABA conductances (Fig. 8E). Along with research outlining the electrotonic compartmentalization of dopamine neurons (Haüsser et al., 1995; Hage and Khaliq, 2015; Moubarak et al., 2019), this suggests a differential contribution to excitatory-inhibitory balance by spatially distributed populations of ACh and GABA inputs from cholinergic axons onto the dendrites of medial SN DA neurons.

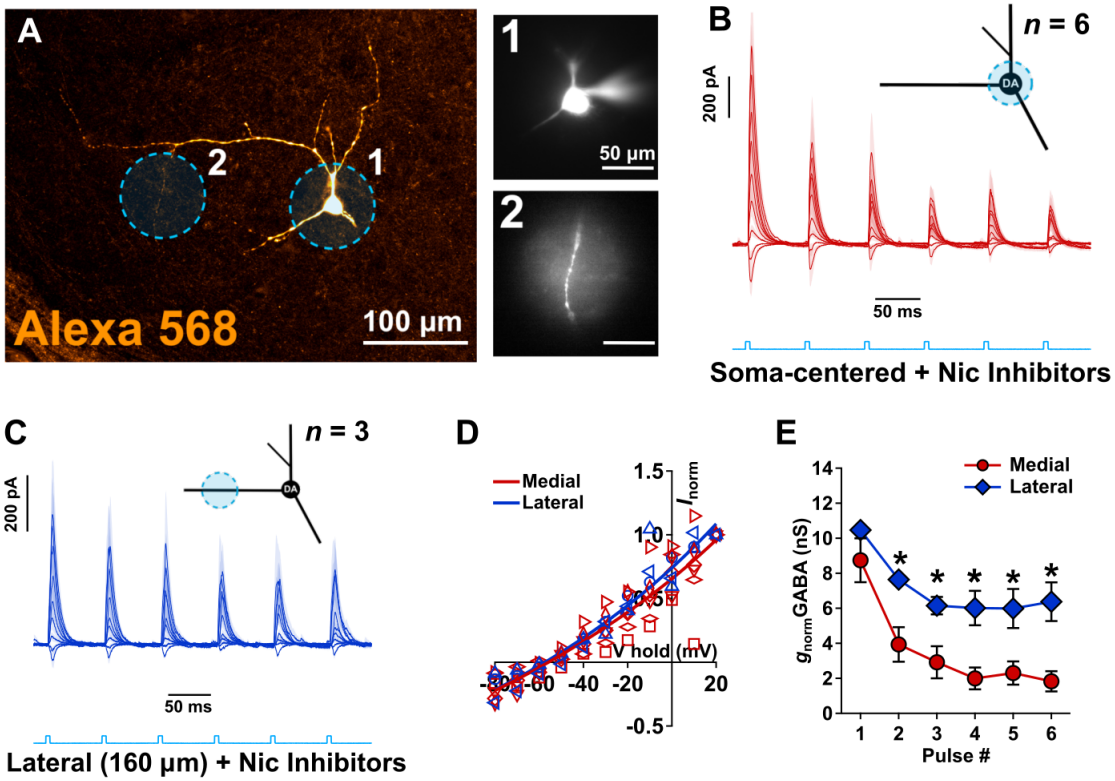

Figure 8. The isolated GABAR conductance is more sustained laterally. A. Experimental design to investigate the isolated GABA conductance from the mix nAChR/GABAR conductance proximally and the primary GABAR conductance laterally. Stimulation fields were restricted to 80 µm. An example DA neuron used in the experiment is shown. **B.** Whole-cell voltage-clamp recordings of local (80 µm) soma-centered GABAR-mediated currents in conditions similar to that of Figure 7. Responses are measured in the presence of CNQX, D-APV, MEC, DHBE, MLA. Mean ± SEM is plotted. **C.** Similar to (B) GABAR currents were measured on a lateral dendrite 160 µm away from the cell body. For **B-C**, $n = 6$ cells from 6 mice, $n = 6$ cells for the proximal focal stimulation, $n = 3$ cells for the lateral focal stimulation (repeated measurements). **D.** The I-V relationships computed from the currents in (B) and (C) and modeled by their respective weighted linear sum of the receptor basis functions as estimated in Figure 4 (thick blue and red lines). The high degree of overlap between fitted I-Vs indicates shows that the voltage clamp data were of adequate quality for the deconvolution procedure. **E.** Normalized estimated medial and lateral GABAR conductances as a function of the pulse number. The lateral GABAR contribution shows less decrease with repeated stimulation compared to the medial GABAR response. Statistical significance $*p < 0.05$, $**p < 0.01$, $***p < 0.001$ was assessed by nonparametric F1-LD-F1 factorial test followed by post-hoc Wilcoxon rank sum tests. Data are shown as mean ± SEM.

Chapter 5 – Discussion

5.1 Summary

The present study investigated the spatial and physiological nature of ACh/GABA co-transmission from brainstem cholinergic axons synapsing onto medial SN DA neurons to understand its role in tuning the neuron's E/I balance. To that end, we have developed a ChR2-based functional input mapping technique with high spatial resolution (~10 μm) and combined local optogenetic stimulation of cholinergic axons with whole-cell patch clamp recordings of DA neurons in *ex-vivo* brain slices from P25-35 mice to probe the dendritic distribution of ACh and GABA release onto DA neurons. Using this technique, we confirmed that medial SN DA neurons receive co-transmitted ACh/GABA monosynaptics (Fig. 3). Notably, we found three different types of monosynaptic transmitter release from cholinergic axons onto DA cells: co-transmitted ACh/GABA, primary GABA, and primary ACh; furthermore, subsequent experiments using immunofluorescent labeling of neurotransmitter vesicular transporters, cholinergic axons, and DA neurons revealed that co-transmission represents a minority of the presynaptic mode of release from cholinergic axons onto medial SN DA neurons, which actually share spatially clustered ACh and GABA-specific cholinergic terminals (Fig. 3, 4, 5, S2). Subpopulations of cholinergic neurons in midbrain cholinergic nuclei, in particular the PPN, are known to possess the cellular machinery for acetylcholine and GABA transmitter release that extends to their presynaptic terminals found in the SN (Estakhr et al., 2017; Li and Spitzer, 2020). We have expanded on those findings by discovering a somatodendritic patterning of cholinergic input distribution onto DA cells with a predominant GABA conductance along the lateral dendrites and a soma-centered ACh/GABA transmission (Fig. 3, 4, 5). While such spatial complexity has been found in other CNS systems (Saunders et al., 2015; Sethuramanujam et al., 2016), such as the retina, this is the first study to date to report the mapping of functional neurotransmitter inputs onto midbrain DA neurons.

Recent optogenetic experiments have shown a dichotomy in the plasticity of ACh and GABA release following activation of cholinergic terminals that are due to differences in release probabilities with low stimulation frequencies (5 Hz) supporting inhibition while high stimulation frequencies (15 Hz) would suggest a shift towards excitation (Estakhr et al., 2017). However, this cellular mechanism did not account for the diversity of distribution of ACh and GABA inputs and the higher proportion of distinct ACh- and GABA-containing cholinergic terminals compared to

co-localized terminals. To investigate the dynamic properties of soma-centered ACh/GABA transmission, we restricted our stimulation field to the cell body in order to measure the contribution of nAChR and GABAR-mediated conductances without recruiting the lateralized population of primary GABA inputs. We then employed a deconvolution method developed by Manookin et al. (2010) to understand the relative plasticity of contributions of nAChRs and GABARs to ACh/GABA transmission onto DA cells. We first quantified full-field isolated voltage-dependent properties of nAChRs and GABARs using a cocktail of receptor antagonists across medial SN DA cells to ensure a high fidelity of deconvolution (Fig. 6). We then modeled the mix I-V relationship as a weighted linear sum of the basis functions for nAChRs and GABARs, which upon deconvolution, yielded an estimate of the fractional conductance for each receptor type at -60 mV across repeated optogenetic stimulations (Fig. 7). We confirmed an initial dominant GABAergic component of ACh/GABA transmission that was previously reported by Estakhr et al. (2017), however, we found that the weight of the GABAergic contribution had a greater decay compared to the ACh component with repeated stimulations, suggesting that a "gate model" of initial inhibition followed a subsequent equalization of excitatory and inhibitory conductances (Fig. 7). We verified the performance of the deconvolution model by bath application of nAChR antagonists which suppressed the associated nAChR conductance (Fig. S4). Finally, we performed similar experiments to compare the short-term plasticity of the isolated GABA conductance during 15 Hz stimulation between the populations of mix ACh/GABA inputs proximally and the population of primary GABA inputs found on the lateral dendrites 160 μm away from the cell body (Fig. 8). Interestingly, the lateral GABA component was more sustained across repeated stimulations compared to the proximal GABA conductance, suggesting a differential contribution to excitation/inhibition balance by spatially distributed populations of ACh and GABA inputs from cholinergic axons onto the dendrites of medial SN DA neurons.

5.2 Spatial Somatodendritic Integration of Functional Synaptic Inputs onto SNc DA Neurons

The way neurons integrate and respond to synaptic inputs depends on the interplay between their morphology, their intrinsic excitability, and the synaptic characteristics of their network (Stuart et al., 2016). Specifically, the distribution of synaptic contacts and their respective location has a significant influence on the neuronal response (Yuste et al., 1994; Williams and Stuart, 2002). This cellular complexity and the dense interconnectivity of the mammalian CNS poses a great

challenge to neuroscientists seeking to decompose neural circuits and ultimately relate them to function (Anastasiades et al., 2018). Fortunately, progress in single and two-photon excitation, neurotransmitter uncaging techniques, and the advent of optogenetics have enabled the development of highly efficient strategies to investigate neuronal connectivity down to the single micron scale (Denk et al., 1990; Denk and Svoboda, 1997; Dalva and Katz, 1994; Dantzker and Callaway, 2000; Nagel et al., 2003; Shepherd et al., 2003, 2005; Boyden et al., 2005; Petreanu et al., 2007, 2009; Jerome and Heck, 2011; Mao et al., 2011). Notably, optogenetic approaches have gained considerable momentum in developing optical mapping techniques (Petreanu et al., 2007, 2009; Mao et al., 2011; D'Souza et al., 2019). However, current approaches have caveats and solutions have often sacrificed throughput for resolution, a longstanding dilemma that microscopists have been all but too familiar with (Petreanu et al., 2007; Little and Carter, 2012; MacAskill et al., 2012; Jin et al., 2020). Here we have developed an optical mapping strategy with small field LED illumination that displayed enhanced resolution (~10 μm) and minimized electrotonic filtering with reduced costs and technical requirements. This is an improvement over the ~100 μm optical stimulation resolution of synaptic input mapping using laser stimulation via a low power (4X) and low numerical aperture (0.16 NA) objective (Petreanu et al 2007). With our technique and complementary immunohistochemical approaches, we provided evidence that a population of SN DA neurons received spatially distributed ACh and GABA-mediated inputs from cholinergic axons. Specifically, optical maps revealed a somatodendritic patterning of input distribution with a predominant GABA conductance on the lateral dendrites and soma-centered ACh/GABA transmission. This has remarkably advanced prior research work from the lab which reported ACh/GABA co-transmission onto those cells (Estakhr et al., 2017). Consistent with Estkahr et al. (2017), cholinergic innervation of DA neurons in the medial SN display ACh/GABA co-transmission centered on the soma and confirmed by the colocalization or close clustering (< 1μm distance) of vesicular ACh and GABA transporters in labeled putative cholinergic terminals; however, this represents the minority of putative presynaptic cholinergic terminals in contrast with individual vesicular GABA and ACh-containing puncta that are found in similar amounts in the vicinity of DA somata, suggesting that the composite ACh/GABA transmission arises from the combinatorial release of ACh and GABA from individual ACh and GABA-containing terminals sharing the same somatodendritic area. This could be explained by two different mechanisms evidenced by prior studies that could act synergistically to mediate axonally distributed ACh and

GABA transmission from cholinergic neurons: (1) evidence from immunolabeling experiments has revealed that a subset of cholinergic neurons in the PPN possess the cellular machinery for both ACh and GABA-mediated transmission and could possess distinct terminals for each transmitter (Estakhr et al., 2017; Li and Spitzer, 2020). Such mechanistic framework is not unforeseen in the CNS; in the retina, starburst amacrine cells can differentially transmit ACh and GABA across their dendritic arbor to drive the directional-selective retinal circuit while in the neocortex, the proportion of layer 1 interneurons that receive ACh or GABA inputs from the same population of cholinergic neurons differs tremendeously, with many cells receiving one of the input types but not the other, suggesting separate vesicle populations for each transmitter (Saunders et al., 2015; Sethuramanujam et al., 2016). Furthermore, (2) neurotransmitter switching from ACh to GABA expression has been revealed to take place in cholinergic PPN neurons that project to the SN and is thought to regulate motor skill learning in mice (Li and Spitzer, 2020).

Neurons with the cellular capability of multi-transmitter signaling can possess various modes of release through differences in presynaptic dynamics coupled to the individual neurotransmitters or differences in the axonal distribution of the individual terminals (Shabel et al., 2014; Saunders et al., 2015; Granger et al., 2016). Similarly, we found three different types of monosynaptic neurotransmitter release from cholinergic axons: co-transmitted ACh/GABA, primary GABA, and primary ACh. Furthermore, while the functional distribution of inputs was sparse across the DA dendrites, suggesting a restricted number of synaptic contacts, input distribution was segregated across the somatodendritic surface with a GABA conductance on lateral DA dendrites.

5.3 Immunohistochemical Mapping of Cholinergic Inputs onto Somatodendritic Regions of DA Neurons

Expanding on the findings by Li and Spitzer (2020) and consistent with our electrophysiological data, a much greater proportion of VGAT+ puncta in labeled cholinergic axons were found within synaptic (< 1 μm) vicinity of the TH+ dendrites lateral to the soma of medial SN DA neurons. This suggests a model of spatially distributed ACh and GABA release that can tremendeously diversify synaptic integration: (1) spatial segregation of excitatory and inhibitory synaptic inputs is a well-known mechanism for overcoming the sublinear summation of PSPs associated with spatiotemporally co-localized signals (Rall, 1959, 1964, 1977; Major et al.,

1994; Bekkers and Stevens, 1996; Stuart and Spruston, 1998; Gentet et al., 2000; Roth and Hausser, 2001); (2) conversely, it could also provide a differential integrative role when taken into account with other transmitter systems (*i.e.,* the lateral GABA conductance could very effectively shunt local glutamatergic inputs from other motor nuclei to code for salient events); and (3) ACh and GABA release could be individually regulated by other neurotransmitter systems that synapse onto the cholinergic terminals, similar to the mechanism evidenced in Glu/GABA co-transmission in the lateral habenula (Shabel et al., 2014; Granger et al., 2016).

Surprisingly, the histological data also revealed that a small proportion of mix ACh/GABA puncta and primary ACh puncta were found 300 μm lateral to the soma of medial SN DA neurons while electrophysiological experiments did not report the presence of an ACh conductance laterally. However, there are a few reasons why such structural findings were not evidenced functionally: (1) The very low proportion of mix ACh/GABA might not be revealed during direct electrophysiological mapping due to the local shunting of the individual conductances combined by the scarcity of synaptic contacts laterally, which would make the PSCs difficult to detect if elicited 300 μm away from the recording electrode, however, the large dorsoventral spread of mix ACh/GABA inputs suggests otherwise and most likely points to (2) ACh and mix ACh/GABA puncta representing a di- or tri-synaptic complex with primary presynaptic modulatory effects which could not be discerned anatomically from a postsynaptic role . This is further suggested by studies reporting that anatomical overlap of axonal projections with dendritic branches does not necessarily correlate with input strength and/or connectivity (Callaway et al., 2002; White, 2002; Petreanu et al., 2009; Mao et al., 2011). Finally, (3) the low proportion of ACh puncta laterally can be easily reconciled based on prior findings observing a heterogeneous cholinergic innervation across SN DA neurons with lateral SN DA neurons primarily receiving ACh-mediated inputs compared to the medial SN DA neuron populations (Estakhr et al., 2017): in this case, the ubiquitous labeling of TH+ dendrites from of all SN DA neurons cannot perfectly resolve the spatial origin of the dendrites with greater distances away from the somata of medial SN DA cells and, considering the large lateral shift of the imaging, could report the VAChT puncta found in the vicinity of DA dendrites originating from neurons found in the lateral SN in contrast with DA dendrites from the medial SN.

5.4 Potential Role of ACh-GABA co-transmission

Changes in the balance between excitation and inhibition has considerable influence on neuronal firing (Denève and Machens, 2016). Spatial segregation of excitatory ACh and inhibitory GABA neurotransmitter release from cholinergic neurons with multi-transmitter capability can lead to differential synaptic effects on the E/I balance (Stuart et al., 2016). While the release of two fast-acting excitatory and inhibitory neurotransmitters might seem functionally antagonistic, co-transmission of ACh and GABA can create graded physiological effects that finely tune the E/I balance in downstream neurons (Granger et al., 2016; Tritsch et al., 2016). Focusing on soma-centered ACh/GABA transmission, we have provided evidence for differential dynamics of ACh and GABA conductances with repeated optical stimulation, suggesting strong initial inhibition followed a subsequent equalization of excitation/inhibition balance. This was in line with recent optogenetic experiments showing a dichotomy in the plasticity of ACh and GABA release following activation of cholinergic terminals that might be due to differences in release probabilities (Estakhr et al., 2017). Interestingly, when considering the isolated transmitter-specific conductance as a function of its spatial dendritic distribution, we found that the lateral GABA component was more sustained across repeated stimulations compared to the proximal GABA conductance. This could be more efficient than anticipated with regards to synaptic integration since previous research have revealed that midbrain DA neurons are electrotonically compact and thus a sustained lateral segregation of inhibition could still help generate efficient shunting, especially considering the variable axonal location (Haüsser et al., 1995; Hage and Khaliq, 2015; Moubarak et al., 2019). Therefore, this suggests a complex differential contribution of E/I balance by spatially distributed populations of ACh and GABA inputs from cholinergic axons onto the dendrites of medial SN DA neurons by virtue of the neurons' morphological and physiological nature.

5.5 Potential Limitations of Optogenetics and Workarounds

Optical stimulation and subcellular mapping have limitations. First, optogenetic experiments can show considerable variability in ChR2 expression and thus alter release probability, especially when using viral vectors (Mao et al., 2011). Fortunately, this can be minimized by using transgenic animals expressing ChR2 (Jackman et al., 2014). In our case, we found increased success by using ChAT-cre female mice for electrophysiological experiments in contrast to male mice, with better and less variable ChR2 expression. However, an under-

appreciated caveat of Cre driver lines is unintentional germline recombination leading to off-target expression of microbial opsins (Luo et al., 2020). Since germline recombination shows a predominant sex-bias with most Cre-driver lines demonstrating greater recombination through the male parent in contrast with the female parent, restricting physiological experiments to female mice and using two different ChAT-cre transgenic mouse lines for electrophysiological and immunohistochemical experiments corroborates the evidence provided in this study, in addition to previous research reporting very low germline recombination efficiency across the ChAT-cre lines (Ray et al., 2018; Luo et al., 2020). Finally, optical mapping is dependent on the quality of the preservation of the dendritic arbor of recorded cells, appropriate spatial clamp, and a high dendritic imaging signal-to-noise ratio, which often requires extended periods of dialysis for targeted optical mapping. To that end, we refined our mapping strategy by ensuring that recorded cells had appropriate dendritic lengths based on prior literature and demonstrated the quality of the voltage clamp by revealing that receptor-specific IVs were space-invariant.

5.6 Future Directions

Based on the data, the primary goal of future experiments would be to investigate the effects of the distributed ACh and GABA release on the firing dynamics of medial SN DA neurons. Specifically, experiments would test whether the sustained GABA conductance laterally would be sufficient to silence neuronal activity at pacemaking potentials compared to the proximal GABA conductance from ACh/GABA transmission. We would also try to understand the role of ACh/GABA transmission with a particular focus on multisynaptic integration. Since the initial data do not reveal a dramatic switch from inhibition to excitation, a more plausible mechanism could involve an interplay between the equalization of net excitatory and inhibitory conductances and the intrinsic voltage-gated properties of the neuron. This could in turn favor an “up” state of DA excitability that would promote EPSP summation and consequent AP firing.

Chapter 6 – Supplemental Information

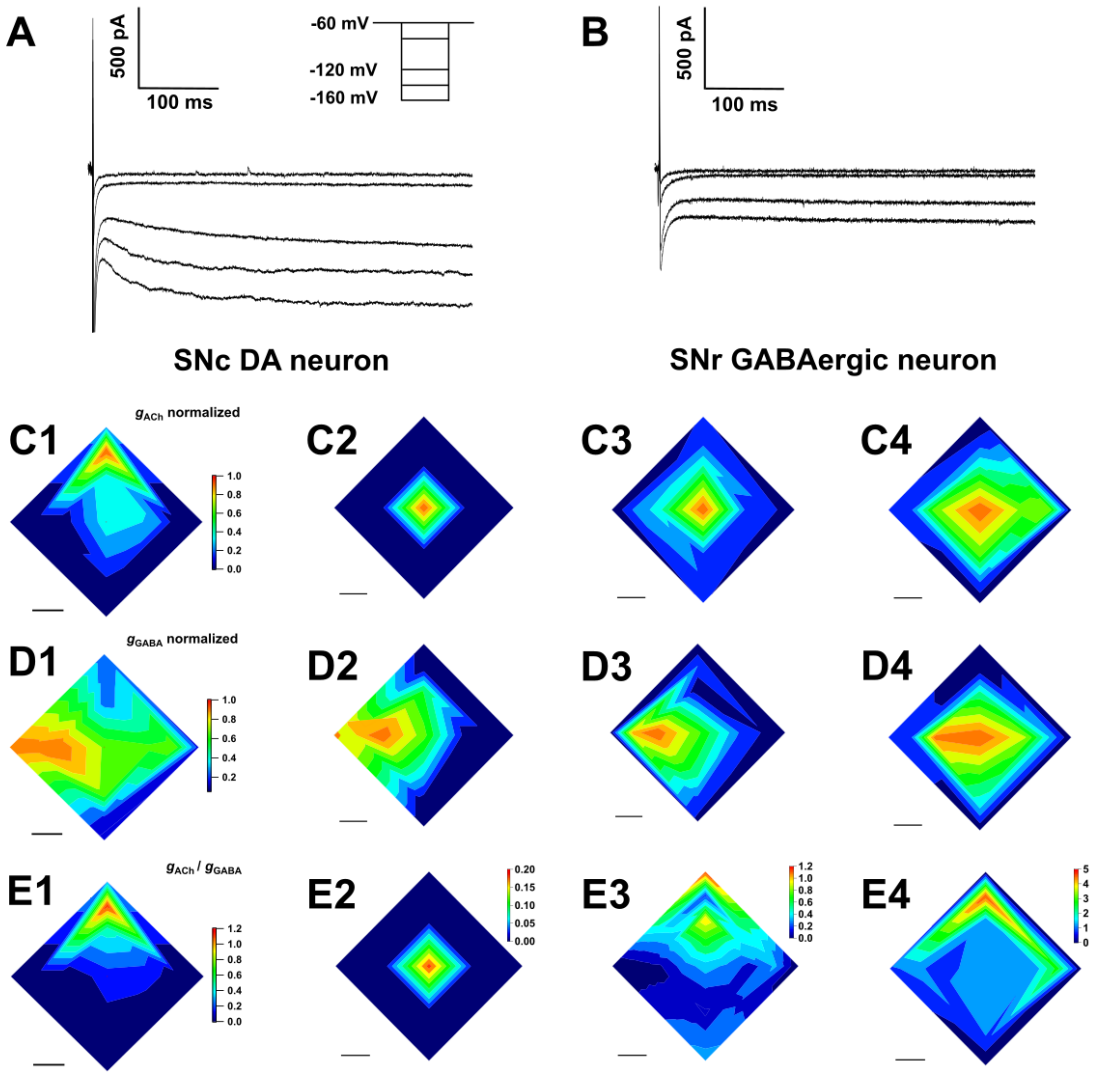

Figure S1. A. Whole-cell voltage-clamp recordings of a SNc DA cell over a range of hyperpolarizing potentials. Note the large HCN-mediated current. **B** Whole-cell voltage-clamp recordings of a SNr GABAergic cell over a range of hyperpolarizing potentials. Note the lack of HCN-mediated current. **C1-4.** Spatial mapping of voltage-isolated light-evoked ACh (recorded at -80 mV) conductances for all four recorded SN DA cells normalized to the maximum ACh conductance. **D1-4** Spatial mapping of voltage-isolated light-evoked GABA (recorded at 0 mV) conductances for all four recorded SN DA cells normalized to the maximum GABA conductance. **E1-4.** Spatial mapping of absolute ACh/GABA conductance ratios for all four recorded SN DA cells. For **C-D**, scale bars are 100 μm.

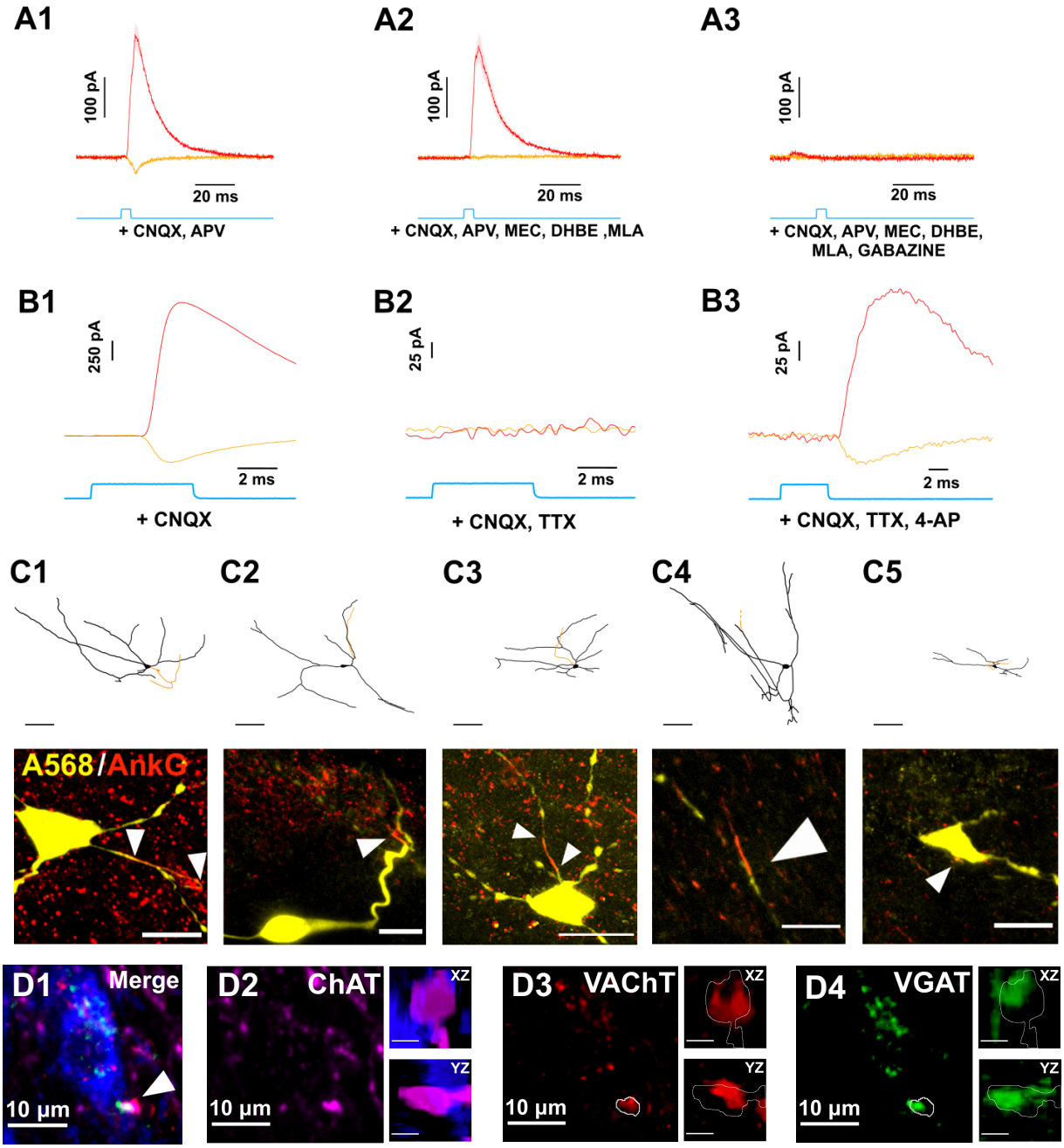

Figure S2. A1-3. Example of light-evoked pharmacologically isolated ACh/GABA PSCs from a medial SN DA neuron. The neuron was voltage-clamped at -55 mV to isolate EPSCs and at 0 mV to isolate IPSCs. All PSCs were recorded in the presence of glutamate receptor antagonists CNQX and D-APV (baseline). ACh PSCs were subsequently supressed using a cocktail of nicotinic receptor antagonists (MLA, DHBE, MEC) and GABA PSCs were supressed with gabazine (from left to right). *n* = 1 cell from 1 mouse. **B1-3.** Example light-evoked PSCs from a medial SN DA neuron voltage-clamped at -90 and 0 mV in the presence of CNQX (baseline) and following subsequent bath application of (left to right) TTX and 4-AP. This indicates that the evoked nicotinic EPSCs and evoked GABA IPSCs are action potential dependent and monosynaptic. *n* = 1 cell from 1 mouse. **C1-5.** Reconstructed medial SN neurons immunostained for Ankyrin G to label the axon initial segment. Scale bar is 15 µm. *n* = 5 cells from 5 mice. **D1-4.** tdTomato cholinergic axon express co-localized VAChT and VGAT in the vicinity of a TH+ DA soma (blue). Insets show *xz* and *yz* projections of the terminal labeled with an arrow. White line marks the fiber outline. Inset scale bars are 2 µm. *n* = 1 cell from 1 mouse.

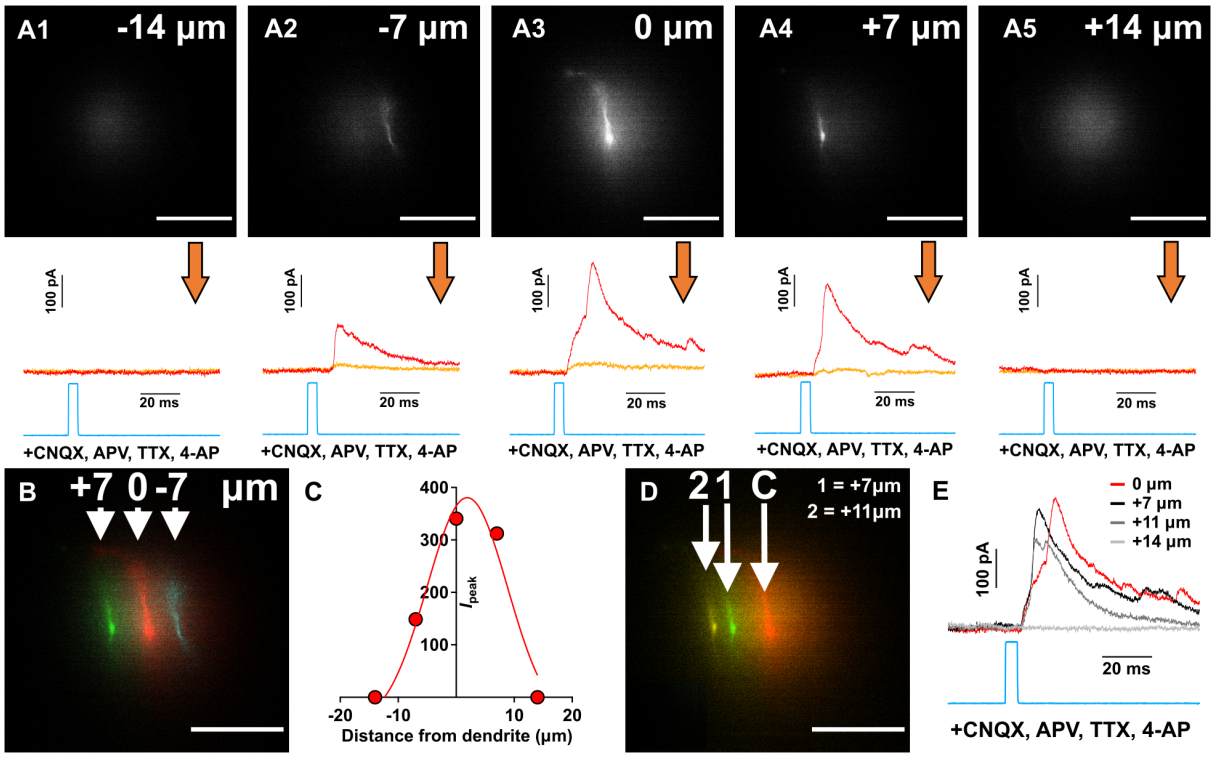

Figure S3. Fine-scale optical mapping resolution and point-spread function. A1-5. Measurement of the point-spread function. Stimulation fields were moved orthogonal to the dendrite excited with Alexa 568 hydrazide (80 µM) in 7 µm increments. Associated whole-cell voltage clamp recordings (-55, 0 mV) in the presence of CNQX, D-APV, TTX, and 4-AP are shown. **B.** Superimposition of imaged lateral shifts relative to the dendrite. Left and right fields were shifted 7 µm relative to the dendritic imaging. Scale bar is 20 µm. **C.** Responses showed in (A) and fitted with a Gaussian function. Half-width was found to be 9.12±3.51 µm and x_0 = 1.88±1.1 µm suggesting that the terminals are found to the right of the dendrite. Mean ± SD is reported. **D.** Further superimposition of imaged lateral shifts relative to the dendrite in the rightward direction as shown in (A). Right fields were shifted 7 and 11 µm relative to the dendritic imaging. Scale bar is 20 µm. **E.** Associated whole-cell voltage clamp recordings at 0 mV for the field shifts shown in (D). Note that peak amplitude was inversely correlated with distance away from the dendrite but no changes in the onset time were observed in the right direction compared to the left direction as shown in (A2). For **A-E**, n = 1 cell from 1 mouse.

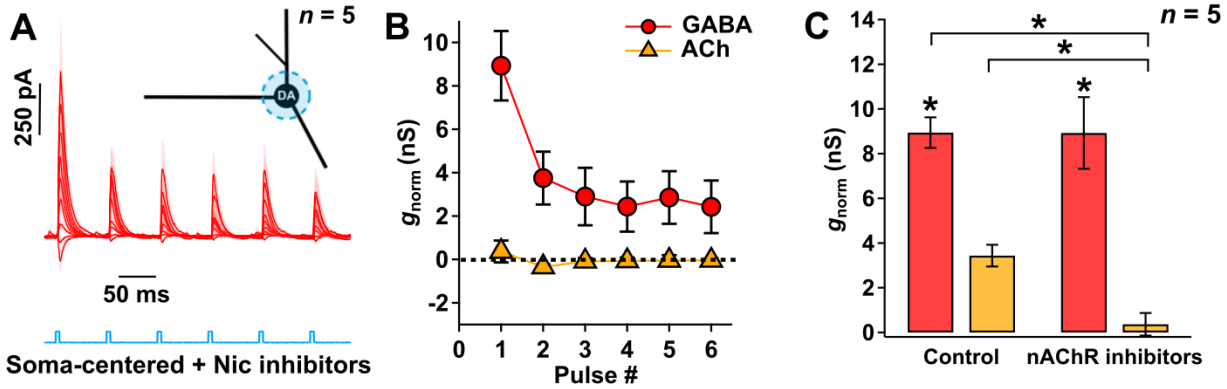

Figure S4. A. Whole-cell voltage-clamp recordings of local (80 µm) soma-centered mix nAChR- and GABAR-mediated currents with repeated ChR2 stimulation (6 pulses, 15 Hz) over a range of holding potentials (-70 to 10 mV, 10 mV increments). Responses are measured in the presence of CNQX, D-APV, MEC, MLA, DHBE, to block AMPA/kainate/NMDARs and nAChRs. $n = 5$ cells from 5 mice, mean ± SEM is plotted. **B.** Normalized estimated ACh and GABA conductances as a function of the pulse number. Note that the estimated gACh across pulses is not significantly different from 0. mean ± SEM is plotted. **C.** Normalized estimated ACh (yellow) and GABA (red) conductances for the first pulse with and without nAChR inhibitors. Statistical significance $*p < 0.05$, $**p < 0.01$, $***p < 0.001$ was assessed by paired Wilcoxon rank sum tests. Data are shown as mean ± SEM.

Table S1. Statistical Analyses, related to Figures 4, 5, 7, 8, S4.

Fig	Sample size (*n*)	Statistical Test	Values
4K	*n* = 148 inputs from 10 neurons, 10 mice	Aligned Rank Transformed (ART) ANOVA with post-hoc pairwise contrast tests for main effects with Tukey correction	ART ANOVA F=30.124, p =3.5491e-15 Pairwise Contrasts: gACh – gGABA, df=144, t.ratio=-4.532, p= 0.0001 gACh–gAChMIX, df=144, t.ratio=-0.842, p= 0.8341 gACh–gGABAMIX, df=144, t.ratio=-6.572, p= <0.0001 gGABA–gAChMIX, df=144, t.ratio=5.654, p= <0.0001 gGABA–gGABAMIX, df=144, t.ratio=-3.567, p= 0.0027 gAChMIX–gGABAMIX, df=144, t.ratio=-8.356, p= <0.0001
5C	*n* = 4 mice, *n* = 6 z-stack images per mouse. Each dot represents one z-stack. *n* = 24 z-stacks per group (VGAT+, VAChT+, VGAT+:VAChT+). *n* = 48 medial z-stacks, *n* = 24 lateral z-stacks.	Linear regression mixed model (Type III ANOVA with Satterthwaite's method) followed by post-hoc pairwise contrast tests for main effects with Tukey correction	Type III Analysis of Variance Table with Satterthwaite's method: Type F=62.996, p=4.973e-16 Location F=0, p=1 Type:Location F=12.582, p=2.348e-05 Pairwise Contrasts (interaction=true): VGAT–VACHT/MED–LAT, df=44, t.ratio=-5.007, p=<0.0001 VGAT–MIX/MED–LAT, df=44, t.ratio=-2.232, p=0.0308 VACHT–MIX/MED–LAT, df=44, t.ratio=2.775, p=0.0081 Degrees-of-freedom method: kenward-roger Pairwise Contrasts: VGAT MED-VACHT MED, df=44, t.ratio=1.799, p=0.4771 VGAT MED-MIX MED, df=44, t.ratio=7.665, p=<0.0001 VGAT MED-VGAT LAT, df=66, t.ratio=-3.412, p=0.0135 VGAT MED-VACHT LAT, df=66, t.ratio=5.137, p=<0.0001 VGAT MED-MIX LAT, df=66, t.ratio=6.002, p=<0.0001 VACHT MED-MIX MED, df=44, t.ratio=5.866, p=<0.0001 VACHT MED-VGAT LAT, df=66, t.ratio=-4.88, p=<0.0001 VACHT MED-VACHT LAT, df=66, t.ratio=3.668, p=0.0063 VACHT MED-MIX LAT, df=66, t.ratio=4.534, p=0.0003 MIX MED-VGAT LAT, df=66, t.ratio=-9.671, p=<0.0001 MIX MED-VACHT LAT, df=66, t.ratio=-1.122, p=0.8707 MIX MED-MIX LAT, df=66, t.ratio=-0.256, p=0.9998 VGAT LAT-VACHT LAT, df=44, t.ratio=7.404, p=<0.0001 VGAT LAT-MIX LAT, df=44, t.ratio=8.153, p=<0.0001 VACHT LAT-MIX LAT, df=44, t.ratio=0.750, p= 0.9743 Degrees-of-freedom method: kenward-roger
5D			Type III Analysis of Variance Table with Satterthwaite's method: Type F=18.874, p=1.207e-06 Location F=11.729, p=0.002424 Type:Location F=4.456, p=0.017289 Pairwise Contrasts (interaction=true): VGAT–VACHT MED–LAT, df=44, t.ratio=-0.220, p=0.8269 VGAT–MIX MED–LAT, df=44, t.ratio=-2.468, p=0.0175 VACHT–MIX MED–LAT, df=44, t.ratio=2.688, p=0.0101 Degrees-of-freedom method: kenward-roger Pairwise Contrasts: VGAT MED-VACHT MED, df=44, t.ratio=2.533, p=0.1368 VGAT MED-MIX MED, df=44, t.ratio=7.458, p=<0.0001 VGAT MED-VGAT LAT, df=44.2, t.ratio=3.543, p=0.0114 VGAT MED-VACHT LAT, df=44.2, t.ratio=5.232, p=<0.0001 VGAT MED-MIX LAT, df=44.2, t.ratio=5.388, p=<0.0001 VACHT MED-MIX MED, df=44, t.ratio=4.925, p=0.0002 VACHT MED-VGAT LAT, df=44.2, t.ratio=2.075, p=0.3186 VACHT MED-VACHT LAT, df=44.2, t.ratio=3.764, p=0.0061

			VACHT MED-MIX LAT, df=44.2, t.ratio=3.920, p=0.0061 MIX MED-VGAT LAT, df=44.2, t.ratio=-0.779, p=0.9696 MIX MED-VACHT LAT, df=44.2, t.ratio=0.909, p=0.9421 MIX MED-MIX LAT, df=44.2, t.ratio=1.065, p=0.8924 VGAT LAT-VACHT LAT, df=44, t.ratio=2.060, p=0.3265 VGAT LAT-MIX LAT, df=44, t.ratio=2.250, p=0.2363 VACHT LAT-MIX LAT, df=44, t.ratio=0.190, p=1.000 Degrees-of-freedom method: kenward-roger
5E	*n* = 4512 puncta, *n* = 24 z-stacks, *n* = 4 mice, *n* = 6 z-stack images per mouse.	Two-sided Welch's *t*-test	F=31.61413, p=1.996659e-08
5F	*n* = 4512 puncta, *n* = 24 z-stacks *n* = 4 mice, *n* = 6 z-stack images per mouse.	Linear regression model followed by post-hoc pairwise contrast tests for main effects with Tukey correction	Analysis of Variance Table: Type F=30.2987, p=3.909e-08 Location F=18.1591, p=2.073e-05 Type:Location F=4.0822, p=0.0434 Pairwise Contrasts (interaction=true): VACHT-VGAT MED-LAT, df=4508, t.ratio=-2.020, p=0.0434 Pairwise Contrasts: VACHT MED-VGAT, df=4508, t.ratio=-5.554, p=<0.0001 VACHT MED-VACHT, df=44.2, t.ratio=-4.165, p=0.0002 VACHT MED-VGAT LAT, df=44.2, t.ratio=-5.677, p=<0.0001 VGAT MED-VACHT LAT, df=44.2, t.ratio=-1.503, p=0.4358 VGAT MED-VGAT LAT, df=44.2, t.ratio=-2.213, p=0.1199 VACHT LAT-VGAT LAT, df=44.2, t.ratio=-0.143, p=0.9990
7D	*n* = 60 conductance estimates, *n* = 5 longitudinal repeated conductances estimates for treatments = 2 (g_{ACh}, g_{GABA}) across 5 cells from 5 mice	Nonparametric F2-LD-F2 factorial test followed by post-hoc paired Wilcoxon rank sum tests	F2-LD-F2 with Wald test: gWeight (ACh, GABA), df=1, z=7.73385, p=5.419505e-03 Pulse Number, df=5, z=1088.520597, p=4.092850e-233 gWeight:Pulse Number, df=5, z=2.269759, p=8.106981e-01 Wilcoxon rank sum test, paired=true, alternative=less AChP1-GABAP1, V=0, p=0.03125 AChP2-GABAP2, V=0, p=0.03125 AChP3-GABAP3, V=1, p=0.0625 AChP4-GABAP4, V=6, p=0.4062 AChP5-GABAP5, V=6, p=0.4062 AChP6-GABAP6, V=1, p=0.0625
8E	*n* = 54 conductance estimates, *n* = 5 longitudinal repeated conductances estimates for conditions = 2 ($g_{GABAMED}$, $g_{GABALAT}$) across 3 ($g_{GABALAT}$) and 5 ($g_{GABAMED}$) cells from 8 mice	Nonparametric F1-LD-F1 factorial test followed by post-hoc paired Wilcoxon rank sum tests	F1-LD-F1 with Wald test: Location, df=1, z=15.83062, p=6.927241e-05 Pulse Number, df=5, z=174.43713, p=8.244844e-36 Location:Pulse Number, df=5, z=38.98352, p=2.393049e-07 F1-LD-F1 with ANOVA test: Location, df=1, z=15.830619, p=6.927241e-05 Pulse Number, df= 1.648391, z=18.239617, p=1.597254e-07 Location:Pulse Number, df= 1.648391,z= 1.858376, p= 1.633400e-01 Wilcoxon rank sum test, paired=false, alternative=less MED1-LAT1, W=5, p=0.179 MED2-LAT2, W=0, p=0.0119 MED3-LAT3, W=1, p=0.02381 MED4-LAT4, W=1, p=0.02381 MED5-LAT5, W=1, p=0.02381 MED6-LAT6, W=1, p=0.02381
S4C	*n* = 20 conductance estimates, *n* = 2	paired Wilcoxon rank sum tests	Wilcoxon rank sum test, paired=true, alternative=less ACh-GABA, V=0, p=0.03125

	treatments (-/+ nAChR inhibitors), *n* = 5 cells from 5 mice		ACh+NicInhib-GABA+NicInhib, V=0, p=0.03125 AChNicInhib-GABA, V=0, p=0.03125 AChNicInhib-ACh, V=0, p=0.03125 Wilcoxon rank sum test, paired=true, alternative=two.sided GABANicInhib-GABA, V=7, p=1

Chapter 7 - Bibliography

Agmon-Snir, H., and Segev, I. (1993). Signal delay and input synchronization in passive dendritic structures. J. Neurophy. *70*, 2066–2085.

Albin, R. L., Young, A. B., and Penney, J. B. (1989). The functional anatomy of basal ganglia disorders. Trends. Neurosci. *12*, 366–375.

Albin, R. L., Reiner, A., Anderson, K. D., Penney, J. B. and Young, A.B. (1990), Striatal and nigral neuron subpopulations in rigid Huntington's disease: Implications for the functional anatomy of chorea and rigidity-akinesia. Ann. Neurol. *27*, 357-365.

Amendola, J., Woodhouse, A., Martin-Eauclaire, M-F., and Goaillard, J.M. (2012). Ca2+/cAMP-sensitive covariation of I_A and I_h voltage dependences tunes rebound firing in dopaminergic neurons. J. Neurosci. *32*, 2166–8.

Anastasiades, P. G., Marques-Smith, A., and Butt, S. J. B. (2018). Studies of cortical connectivity using optical circuit mapping methods. J. Physiol. *596*, 145-162.

Andén, N.-E., Dahlström, A., Fuxe, K., Larsson, K., Olson, L., and Ungerstedt, U. (1966). Ascending monoamine neurons to the telencephalon and diencephalon. Acta physiol. scand. *67*, 313-326

Anderson, M. E., and Turner, R. S. (1991). Activity of neurons in cerebellar-receiving and pallidal-receiving areas of the thalamus of the behaving monkey. J. Neurophysiol. *66*, 879–893.

Beckstead, M. J., Grandy, D. K., Wickman, K., and Williams, J. T. (2004). Vesicular dopamine release elicits a ninhibitory postsynaptic current in midbrain dopamine neurons. Neuron. *42*, 939–46.

Beeler, J.A., and Kisbye Dreyer, J. (2019). Synchronicity: the role of midbrain dopamine in whole-brain coordination. eNeuro. *6*.

Bekkers, J. M., and Stevens, C.F. (1996). Cable properties of cultured hippocampal neurons determined from sucrose-evoked miniature EPSCs. J. Neurophysiol. *75*, 1250–1255.

Bhatia, A., Moza, S., and Bhalla, U. S. (2019). Precise excitation-inhibition balance controls gain and timing in the hippocampus. eLife *8.*

Bishop, G. H. (1956). Natural history of the nerve impulse. Physiol. Rev. *36*, 376-99.

Bishop, G. H. (1958). The dendrite: receptive pole of the neurone. Neurophysiol. Suppl. *10,* 12-21.

Bormann, J., Hamill O. P., and Sakmann, B. (1987). Mechanism of anion permeation through channels gated by glycine and gamma-aminobutyric acid in mouse cultured spinal neurones. J. Physiol. *385*, 243–286.

Bossy, B., Ballivet, M. and Spierer, P. (1988). Conservation of neural nicotinic acetylcholine receptors from Drosophila to vertebrate central nervous systems. J. EMBO. *7*, 611-618.

Boyden, E. S., Zhang, F., Bamberg, E., Nagel, G., and Deisseroth, K. (2005). Millisecond timescale, genetically targeted optical control of neural activity. Nat. Neurosci. *8*, 1263–1268

Brown, C.E., Sweetnam, D., Beange, M., Nahirney, P. C., and Nashmi., R. (2012). alpha4* Nicotinic acetylcholine receptors modulate experience-based cortical depression in the adult mouse somatosensory cortex. J. Neurosci. *32*, 1207-1219.

Brunner, E., Domhof, S., and Langer, F. (2002). Nonparametric analysis of longitudinal data in factorial experiments. John Wiley & Sons, New York.

Callaway, E. M. (2002). Cell type specificity of local cortical connections. J. Neurocytol. *31*, 231–37

Callaway, E. M., and Yuste, R. (2002). Stimulating neurons with light. Curr. Opin. Neurobiol. *12*, 587–592.

Cash, S., and Yuste, R. (1999). Linear summation of excitatory inputs by CA1 pyramidal neurons. Neuron *22*, 383–394.

Case, D. T., Burton, S. D., Gedeon, J. Y., Williams, S.-P. G., Urban, N. N., and Seal, R. P. (2017). Layer- and cell type-selective co-transmission by a basal forebrain cholinergic projection to the olfactory bulb. Nat. Commun. *8*, 652.

Chen, B. T., and Rice, M. E. (2001). Novel Ca2+dependence and time course of somatodendritic dopamine release: substantia nigra versus striatum. J. Neurosci. *21*,7841–47.

Clarke, P. B., Hommer, D. W., Pert, A., and Skirboll, L. R. (1987). Innervation of substantia nigra neurons by cholinergic afferents from pedunculopontine nucleus in the rat: neuroanatomical and electrophysiological evidence. Neurosci. *23*, 1011–1019.

Coddington, L. T., and Dudman, J. T. (2019). Learning from action: reconsidering movement signaling in midbrain dopamine neuron activity. Neuron. *104*, 63–77.

Colangelo, C., Schichkova, P., Keller, D., Markram, H., and Ramaswamy, S. (2019). Cellular, synaptic and network effects of acetylcholine in the neocortex. Front. Neural Circuits. *13*, 24.

Colbert, C. M., and Johnston, D. (1996). Axonal action-potential initiation and Na^+ channel densities in the soma and axon initial segment of subicular Pyramidal Neurons. J. Neurosci. *16,* 6676-6686.

Cornwall, J., Cooper, J.D., and Phillipson, O.T. (1990). Afferent and efferent connections of the laterodorsal tegmental nucleus in the rat. Brain Res. Bull. *25*, 271–284.

Dale, H. H. (1914). The action of certain esters and ethers of choline, and their relation to muscarine. J. Pharmacol. Exp. Ther. *6*, 147–190.

Dalva, M. B., and Katz, L. C. (1994). Rearrangements of synaptic connections in visual cortex revealed by laser photostimulation. Science. *265*, 255–258.

Damier P., Hirsch, E. C., Agid, Y., and Graybiel, A. M. (1999). The substantia nigra of the human brain. II. Patterns of loss of dopaminergic neurons in Parkinson's disease. Brain. *122*, 1437–48.

Dantzker, J. L., and Callaway, E. M. (2000). Laminar sources of synaptic input to cortical inhibitory interneurons and pyramidal neurons. Nat. Neurosci. *3*, 701–707.

Dembrow, N. C., and Zemelman, B. V. (2015). Temporal dynamics of L5 dendrites in medial prefrontal cortex regulate integration versus coincidence detection of afferent inputs. J. Neurosci. *35*, 4501–4514.

Denève S., and Machens, C. K. (2016). Efficient codes and balanced networks. Nat. Neurosci. *19*, 375–382.

Deniau, J. M., Mailly, P., Maurice, N., and Charpier, S. (2007). The pars reticulata of the substantia nigra: a window to basal ganglia output. Prog. Brain Res. *160*, 151–172.

Denk, W., Strickler, J. H., and Webb, W. W. (1990). Two-photon laser scanning fluorescence microscopy. Science. *248*,73–76.

Denk, W., and Svoboda, K. (1997). Photon upmanship: why multiphoton imaging is more than a gimmick. Neuron *18*,351–357.

Descarries, L., and Mechawar, N. (2000). Ultrastructural evidence for diffuse transmission by monoamine and acetylcholine neurons of the central nervous system. In *Progress in Brain Research* eds L. F. Agnati, K. Fuxe, C. Nicholson and Syková E. (Amsterdam: Elsevier), 27–47.

Donkelaar, H. J. T., and ten Donkelaar, H. J. (2009). Evolution of motor systems: corticospinal, reticulospinal, rubrospinal and vestibulospinal systems. In Encyclopedia of Neuroscience, M.D. Binder, N. Hirokawa, and U. Windhorst, eds. (Springer), 1248–1254.

Drenan, R. M. et al. (2008). *In vivo* activation of midbrain dopamine neurons via sensitized, high-affinity α6 nicotinic acetylcholine receptors. Neuron. *60*, 123–136.

Drenan, R. M., Grady, S. R., Steele A. D., McKinney S., Patzlaff, N.E., et al. (2010). Cholinergic modulation of locomotion and striatal dopamine release is mediated by alpha6alpha4* nicotinic acetylcholine receptors. J Neurosci. *30*, 9877–89.

D'Souza, R. D., Bista, P., Meier, A. M., Ji, W. and Burkhalter, A. (2019). Spatial clustering of inhibition in mouse primary visual cortex. Neuron. *104*, 588–600.

Dudman, J. T., and Gerfen, C. R. (2015). The Basal Ganglia, Fourth Edition (The Rat Nervous System).

Eccles, J. C., Fatt, P., and Koketsu, K. (1953). Cholinergic and inhibitory synapses in a central nervous pathway. Aust. J. Sci.*16*, 50–54.

Eccles, J. C., Fatt, P., and Koketsu, K. (1954). Cholinergic and inhibitory synapses in a pathway from motor-axon collaterals to motoneurones. J. Physiol. *126*,524–562.

Eccles, J. C. (1960). The properties of the dendrites. Amsterdam: Elsevier.

Eccles, J.C. (1964). The physiology of synapses. Berlin: Springer-Verlag.

Eccles, J. C. (1976). From electrical to chemical transmission in the central nervous system. Notes Rec. R. Soc. Lond. *30*, 219–230.

Estakhr, J., Abazari, D., Frisby, K., McIntosh, J. M., and Nashmi, R. (2017). Differential control of dopaminergic excitability and locomotion by cholinergic inputs in mouse substantia nigra. Curr. Biol. *27*, 1900–1914.

Evans, R. C., Zhu, M., Khaliq, Z. M. (2017). Dopamine inhibition differentially controls excitability of SNc dopamine neuron subpopulations through recruitment of T-type calcium channels. J. Neurosci. *37*, 3704–20

Fallon J. H., Loughlin S. E. (1975). Substantia nigra. In *The Rat Central Nervous System*, ed. G Paxinos, New York: Academic. 215–37.

Fatt, P., and Katz, B. (1952). Spontaneous subthreshold activity at motor nerve endings. J. Physiol. *117*, 109-128.

Fatt, P., and Katz, B. (1953). The effect of inhibitory nerve impulses on a crustacean muscle fibre. J. Phvsiol., *121*, 374-389.

Fearnley, J. M., and Lees, A. J. (1991). Ageing and Parkinson's disease: substantia nigra regional selectivity. Brain. *114*, 2283–2301.

Fu, Y., Yuan, Y., Halliday, G., Ruszna´ K. Z., Watson, C., and Paxinos, G. (2012). A cytoarchitectonic and chemoarchitectonic analysis of the dopamine cell groups in the substantia nigra, ventral tegmental area, and retrorubral field in the mouse. Brain Struct. Funct. *217*, 591–612.

Fujita, Y. (1968). Activity of dendrites of single Purkinje cells and its relationship to so-called inactivation response in rabbit cerebellum. J. Neurophysiol. *31*, 131–141.

Futami T., Takakusaki K., Kitai, S.T. (1995). Glutamatergic and cholinergic inputs from the pedunculopontine tegmental nucleus to dopamine neurons in the substantia nigra pars compacta. Neurosci Res *21*, 331–342.

Galtieri, D.J., Estep, C.M., Wokosin, D.L., Traynelis, S., Surmeier, D.J., (2017). Pedunculopontine glutamatergic neurons control spike patterning in substantia nigra dopaminergic neurons. elife. *6.*

Gantz, S. C., Ford, C. P., Morikawa, H., and Williams, J. T. (2018). The evolving understanding of dopamine neurons in the substantia nigra and ventral tegmental area. Annu. Rev. Physiol. *80*, 219–241.

Geisler, S., Derst, C., Veh, R.W., and Zahm, D. S. (2007). Glutamatergic afferents of the ventral tegmental area in the rat. J. Neurosci. *27*, 5730–5743.

Gentet, L. J., Stuart G. J., and Clements J.D. (2000). Direct measurement of specific membrane capacitance in neurons. Biophys. J. *79*, 314–320.

Gerfen, C. R., Engber, T. M., Mahan, L. C., Susel, Z., Chase, T. N., Monsma, F. J. Jr., and Sibley, D. R. (1990). D1 and D2 dopamine receptor-regulated gene expression of striatonigral and striatopallidal neurons. Science. *250*,1429–1432.

Gerfen, C., and Surmeier, D. (2010). Dichotomous modulation of striatal direct and indirect pathway neurons by dopamine. Annu. Rev. Neurosci. *34*, 441–466.

Gerschenfeld H. M. (1973). Chemical transmission in invertebrate central nervous system and neuromuscular junctions. Physiological Reviews. *53,* 1-119.

Goldberg, J.H., and Fee, M.S. (2012). A cortical motor nucleus drives the basal ganglia-recipient thalamus in singing birds. Nat. Neurosci. *15*, 620–627.

Gonon, F., and Bloch, B. (1998). Kinetics and geometry of the excitatory dopaminergic transmission in the rat striatum in vivo. Adv Pharmacol. *42*,140–144.

Grace, A. A., and Bunney, B. S. (1984a). The control of firing pattern in nigral dopamine neurons: single spike firing. J. Neurosci.4, 2866–2876.

Grace, A. A., and Bunney, B. S. (1984b). The control of firing pattern in nigral dopamine neurons: burst firing. J. Neurosci.*4,* 2877–2890.

Granger, A. J., Mulder, N., Saunders, A. and Sabatini, B. L. (2016). Cotransmission of acetylcholine and GABA. Neuropharmacology. *100*, 40–46.

Gras, C., et al. (2008). The vesicular glutamate transporter VGLUT3 synergizes striatal acetylcholine tone. Nat. Neurosci. *11*, 292–300.

Guerriero, R. M., Giza, C. C., and Rotenberg, A. (2015). Glutamate and GABA imbalance following traumatic brain injury. Curr. Neurol. Neurosci. Rep. *15,* 27.

Guillem, K., Bloem, B., Poorthuis, R. B., Loos, M., Smit, A. B., Maskos, U., Spijker, S., and Mansvelder, H. D. (2011). Nicotinic acetylcholine receptor beta2 subunits in the medial prefrontal cortex control attention. Science. *333*, 888-891.

Guzman, J. N., Sànchez-Padilla, J., Chan, C. S., and Surmeier, D. J. (2009). Robust pacemaking in substantia nigra dopaminergic neurons. J. Neurosci. *29*, 11011–11019.

Guzman, M. S., et al. (2011). Elimination of the vesicular acetylcholine transporter in the striatum reveals regulation of behaviour by cholinergic-glutamatergic co-transmission. PLoS Biol. *9.*

Haber, S.N. (2003). The primate basal ganglia: parallel and integrative networks. J. Chem. Neuroanat. *26*, 317–330.

Hage, T. A., and Khaliq, Z. M. (2015). Tonic firing rate controls dendritic Ca2+ signaling and synaptic gain in substantia nigra dopamine neurons. J. Neurosci. *35*, 5823–36.

Hage, T. A., Sun, Y., and Khaliq, Z. M. (2016). Electrical and Ca2+ signaling in dendritic spines of substantia nigra dopaminergic neurons. eLife. *5*.

Haghighi, A. P., and Cooper, E. (1998). Neuronal nicotinic acetylcholine receptors are blocked by intracellular spermine in a voltage-dependent manner. J Neurosci *18*, 4050–4062.

Hammond C, Deniau J. M., Rizk A., and Féger, J. (1978) Electrophysiological demonstration of an excitatory subthalamonigral pathway in the rat. Brain Res *151*, 235–244.

Hammond, C. (2015). Cellular and molecular neurophysiology. 4th ed, Academic Press.

Hansen, S. B., Taylor, P., Sulzenbacher, G., Bourne, Y., Huxford, T., and Marchot, P. (2005). Structures of aplysia AChBP complexes with nicotinic agonists and antagonists reveal distinctive binding interfaces and conformations. EMBO J. *24*, 3635-3646.

Häusser, M., Stuart, G., Racca, C., and Sakmann, B. (1995). Axonal initiation and active dendritic propagation ofaction potentials in substantia nigra neurons. Neuron. *15*, 637–47.

Henny, P., et al. (2012). Structural correlates of heterogeneous *in vivo* activity of midbrain dopaminergic neurons. Nat. Neurosci. *15*, 613–19.

Hnasko, T. S., and Edwards, R. H. (2012). Neurotransmitter corelease: mechanism and physiological role. Annu. Rev. Physiol. *74,* 225–243.

Hodgkin, A. L., and Huxley, A. F. (1952). A quantitative description of membrane current and its application to conduction and excitation in nerve. J. Phvsiol. *117*, 500-544.

Jackman, S. L., Beneduce, B. M., Drew, I. R. and Regehr, W. G. (2014). Achieving high-frequency optical control of synaptic transmission. J. Neurosci. *34*, 7704–7714.

Jaffe, D. B., and Carnevale, N. T. (1999). Passive normalization of synaptic integration influenced by dendritic architecture. J. Neurophysiol. *82*, 3268–3285.

Jerome, J., and Heck, D. H. (2011). The age of enlightenment: evolving opportunities in brain research through optical manipulation of neuronal activity. Front. Syst. Neurosci. *5*, 95.

Jin, L., Liu, B., Zhao, F. et al. (2020). Deep learning enables structured illumination microscopy with low light levels and enhanced speed. Nat Commun *11*, 1934.

Kabanova, A. et al. (2015). Function and developmental origin of a mesocortical inhibitory circuit. Nat. Neurosci. *18*, 872–882.

Kaczorowski, C. C., Disterhoft, J. and Spruston, N. (2007), Stability and plasticity of intrinsic membrane properties in hippocampal CA1 pyramidal neurons: effects of internal anions. J. Physiol.*578*: 799-818.

Kalmbach, A., Hedrick, T., and Waters, J. (2012). Selective optogenetic stimulation of cholinergic axons in neocortex. J. Neurophysiol. *107*, 2008–2019

Kandel, E. R., Schwartz, J. H., Jessell, T. M., Siegelbaum, S. A., and Hudspeth, A. J. (2012). Principles of Neural Science, Fifth Edition (McGraw HillProfessional).

Káradóttir, R., and Attwell, D. (2006). Combining patch-clamping of cells in brain slices with immunocytochemical labeling to define cell type and developmental stage. Nat. Protoc. *1*, 1977–1986.

Karczmar AG. (2007). Exploring the vertebrate central cholinergic system. New York: Springer.

Kemp, J. M. and Powell, T. P. S. (1970). The cortico-striate projection in the monkey, Brain. *93*, 525–546.

Kita H., and Kitai, S. T. (1987). Efferent projections of the STN in the rat: light and electron microscopic analysis with the PHA-L method. J. Comp. Neurol. *260*, 435–452.

Koch, C., Rapp, M., and Segev, I. (1996). A brief history of time (constants). Cereb Cortex *6*, 93–101.

Kornhuber, J., Kim, J. S., Kornhuber, and M.E., Kornhuber, H.H. (1984). The cortico-nigral projection: Reduced glutamate content in the substantia nigra following frontal cortex ablation in the rat. Brain Res. *322*, 124 – 126.

Lee C.R., and Tepper J.M. (2009). Basal Ganglia Control of Substantia Nigra Dopaminergic Neurons. In: Giovanni G., Di Matteo V., Esposito E. (eds) Birth, Life and Death of Dopaminergic Neurons in the Substantia Nigra. Journal of Neural Transmission. *73*, Springer.

Lee, S., Kim, K. and Zhou, Z. J. (2010) Role of ACh–GABA cotransmission in detecting image motion and motion direction. Neuron. *68*, 1159–1172.

Leung, J., McPhee, D. M., Renda, A., Penty, N., Farhoomand, F., Nashmi, R. and Delaney, K. R. (2017). MeCP2-deficient mice have reduced alpha4 and alpha6 nicotinic receptor mRNA and altered behavioral response to nicotinic agonists. Behavorial Brain Res. *330*, 118-126.

Li, X. et al. (2005). Fast noninvasive activation and inhibition of neural and network activity by vertebrate rhodopsin and green algae channelrhodopsin. Proc. Natl Acad. Sci. USA. *102*, 17816–17821 (2005).

Li, H., and Spitzer, N. C. (2020). Exercise enhances motor skill learning by neurotransmitter switching in the adult midbrain. Nat Commun. *11*, 2195.

Lin, J.Y. (2011). A user's guide to channelrhodopsin variants: features, limitations and future developments. Exp. Physiol. *96,* 19–25.

Liss, B., Frans, O., Sewing, S., Bruns, R., Neuhoff, H., et al. (2001). Tuning pacemaker frequency of individual dopaminergic neurons by Kv4.3L and KChip3.1 transcription. EMBO J. *20*, 5715–24.

Little, J. P., and Carter, A. G. (2012). Subcellular synaptic connectivity of layer 2 pyramidal neurons in the medial prefrontal cortex. J. Neurosci. *32*, 12808–12819.

Llinàs, R., Nicholson, C., Freeman, J. A., and Hillman, D. E. (1968). Dendritic spikes and their inhibition in alligator Purkinje cells. Sci. *160*, 1132–1135.

Llinàs, R., and Hess, R. (1976). Tetrodotoxin-resistant dendritic spikes in avian Purkinje cells. Proc. Natl. Acad. Sci. *73*, 2520–2523.

Llinàs, R., and Sugimori, M. (1980). Electrophysiological properties of in-vitro Purkinje cell somata in mammalian cerebellar slices. J. Physiol. *305*, 171–195.

Loewi, O. (1924). Pflügers Archive *204*, 629-640.

Lowell, B. B., et al. (2006) Development and phenotype of ChAT-IRES-Cre mice. MGI Direct Data Submission.

Ludwig, M., and Leng, G. (2006). Dendritic peptide release and peptide-dependent behaviours. Nat. Rev. Neurosci.*7*, 126–136.

Luo, L., Callaway, E. M., and Svoboda, K. (2008). Genetic dissection of neural circuits. Neuron *57*, 634–660.

Luo, L. et al. (2020). Optimizing nervous system-specific gene targeting with Cre driver lines: prevalence of germline recombination and influencing factors. Neuron. *106*, 37–65

Luquin, E., Huerta, I., Aymerich, M. A., and Mengual, E. (2018) Stereological estimates of glutamatergic, GABAergic, and cholinergic neurons in the pedunculopontine and laterodorsal tegmental nuclei in the rat. Front Neuroanat *12*,34.

MacAskill, A. F., Little, J. P., Cassel, J. M., Carter, A. G. (2012) Subcellular connectivity underlies pathway-specific signaling in the nucleus accumbens. Nat Neurosci *15*, 1624–1626.

Madisen, L., et al. (2010). A robust and high-throughput Cre reporting and characterization system for the whole mouse brain. Nat. Neurosci. *13*, 133–140.

Madisen, L., et al. (2012). A toolbox of Cre-dependent optogenetic transgenic mice for light-induced activation and silencing. Nat Neurosci. *15*, 793-802.

Magee J. C. (2000). Dendritic integration of excitatory synaptic inputs. Nat. Rev. Neurosci. *1*, 181– 90.

Manookin, M. B., Weick, M., Stafford, B. K., and Demb, J. B. (2010) NMDA receptor contributions to visual contrast coding. Neuron *67*, 280 –293.

Mao, T., Kusefoglu, D., Hooks, B. M., Huber, D., Petreanu, L., and Svoboda, K. (2011). Long-range neuronal circuits underlying the interaction between sensory and motor cortex. Neuron *72*, 111–123.

Matsuma, M., Watanabe, K., and Ohye, C. (1997). Single-unit activity in the primate nucleus tegmenti pedunculopontine related to voluntary arm movement. Neurosci Rev. *28*, 155-65.

McHaffie, J. G., Jiang, H., May, P. J., Coizet, V., Overton, P. G., Stein, B. E., Redgrave, P. (2006). A direct projection from superior colliculus to substantia nigra pars compacta in the cat. Neuroscience. *138*, 221-234.

McGuire, J. L., Ngwenya, L. B., and Mccullumsmith, R. E. (2019). Neurotransmitter change after traumatic brain injury: an update for new treatment strategies. Mol. Psychiatry. *24,* 995-1012.

Mena-Segovia, J., and Bolam, J. P. (2017). Rethinking the pedunculopontine nucleus: from cellular organization to function. Neuron. *94*, 7–18.

Mink, J. W. (1996). The basal ganglia: focused selection and inhibition of competing motor programs. Prog Neurobiol. *50*, 381–425

Miyazawa, A., Fujiyoshi, Y. and Unwin, N. 2003. Structure and gating mechanism of the acetylcholine receptor pore. Nature. *423*, 949–955.

Moubarak, E., Engel, D., Dufour, M. A., Tapia, M., Tell, F., and Goaillard, J.-M. (2019). Robustness to axon initial segment variation is explained by somatodendritic excitability in rat substantia nigra dopaminergic neurons. J. Neurosci. *39*, 5044–5063.

Muñoz, W., and Rudy, B. (2014). Spatiotemporal specificity in cholinergic control of neocortical function. Curr. Opin. Neurobiol. *26*, 149–160.

Nagel, G., Szellas, T., Huhn, W., Kateriya, S., Adeishvili, N., Berthold, P., Ollig, D., Hegemann, P., and Bamberg, E. (2003). Channelrhodopsin-2, a directly light-gated cation-selective membrane channel. Proc Natl Acad Sci USA *100*,13940–13945.

Nagel, G. et al. (2005). Light activation of channelrhodopsin-2 in excitable cells of *Caenorhabditis elegans* triggers rapid behavioral responses. Curr. Biol. *15*, 2279–2284.

Nashmi R., and Lester H. A. (2006). CNS localization of neuronal nicotinic receptors. J. Mol. Neurosci. *30*, 181–184.

Nashmi, R., Xiao, C., Deshpande, P., McKinney, S., Grady, S. R., Whiteaker, P., . . . Lester, H. A. (2007). Chronic nicotine cell specifically upregulates functional alpha 4 nicotinic receptors: Basis for both tolerance in midbrain and enhanced long-term potentiation in perforant path. J. Neurosci. *27*, 8202.

Nasirova, N., Quina, L. A., Agosto-Marlin, I. M., Ramirez, J., Lambe, E. K., and Turner, E. E. (2020). Dual recombinase fate mapping reveals a transient cholinergic phenotype in multiple populations of developing glutamatergic neurons. J. Comp. Neurol. *528*,283–307.

Obermayer J., Luchicchi A., Heistek T. S., de Kloet S. F., Terra H., Bruinsma B., et al. (2019). Prefrontal cortical ChAT-VIP interneurons provide local excitation by cholinergic synaptic transmission and control attention. Nat Commun. *10*, 5280.

Okada, K., and Kobayashi, Y. (2015). Rhythmic firing of pedunculopontine tegmental nucleus neurons in monkeys during eye movement task. PLoS ONE. *10*

Paxinos, G., and Franklin, K. (2019) The Mouse Brain in Stereotaxic Coordinates. Fifth edition. Academic Press.

Parent, A., Mackey, A., Smith, Y., and Boucher, R. (1983). The output organization of the substantia nigra in primate as revealed by a retrograde double labeling method. Brain Res. Bull.*10*, 529–537.

Perez-Lloret, S., and Barrantes, F. J. (2016). Deficits in cholinergic neurotransmission and their clinical correlates in Parkinson's disease. NPJ Parkinsons Dis. *2*, 16001.

Petreanu, L., Huber, D., Sobczyk, A., and Svoboda, K. (2007). Channelrhodopsin-2-assisted circuit mapping of long-range callosal projections. Nat. Neurosci. *10*, 663–668.

Petreanu, L., Mao, T., Sternson, S. M., and Svoboda, K. (2009). The subcellular organization of neocortical excitatory connections. Nature. *457*, 1142–1145.

Phillips, J.W., et al. (2018). A single spectrum of neuronal identities across thalamus. BioRxiv.

Phillipson, O. T. (1979). A Golgi study of the ventral tegmental area of Tsai and interfascicular nucleus in the rat. J. Comp. Neurol. *187*, 99–116.

Puopolo, M., Raviola, E., and Bean, B. P. (2007). Roles of subthreshold calcium current and sodium current in spontaneous firing of mouse mid-brain dopamine neurons. J. Neurosci. *27*, 645–656.

Rall, W. (1958) Mathematical solutions for passive electrotonic spread between a neuron soma and its dendrites. Federation Proc. *17*, 127.

Rall, W. (1962), Theory of physiological properties of dendrites. Annals N. Y. Ac. Sci. *96*, 1071-1092.

Rall, W. (1964) Theoretical significance of dendritic trees for neuronal input-output relations. Stanford Univ. Press.

Rall W. (1977). Core conductor theory and cable properties of neurons. In: Handbook of physiology. The nervous system. Cellular biology of neurons. Bethesda, MD: American Physiology Society, 39–97.

Rasmussen, G. L. (1957). Selective silver impregnation of synaptic endings. In: New Research Techniques of Neuroanatomy, W. F. Windle, ed., Springfield, Ill.: C. C Thomas.

Ray, T. A., Roy, S., Kozlowski, C., Wang, J., Cafaro, J., Hulbert, S. W., Wright, C. V., Field, G. D., and Kay, J. N. (2018). Formation of retinal direction-selective circuitry initiated by starburst amacrine cell homotypic contact. eLife. *7*.

Redgrave, P., Rodriguez, M., Smith, Y. et al. (2010). Goal-directed and habitual control in the basal ganglia: implications for Parkinson's disease. Nat Rev Neurosci. *11*, 760–72.

Rice, M. E., and Patel, J. C. (2015). Somatodendritic dopamine release: recent mechanistic insights. Phil. Trans.R. Soc. B. *370*.

Rinvik E., and Ottersen, O.P. (1993). Terminals of subthalamonigral fibres are enriched with glutamate-like immunoreactivity: an electron microscopic, immunogold analysis in the cat. J. Chem. Neuroanat. *6*, 19–30.

Rossi, J. et al. (2011). Melanocortin-4 receptors expressed by cholinergic neurons regulate energy balance and glucose homeostasis. Cell. Metab. *13*, 195–204.

Roth, A., and Häusser, M. (2001). Compartmental models of rat cerebellar Purkinje cells based on simultaneous somatic and dendritic patch-clamp recordings. J. Physiol. *535*, 445–472.

Sarter, M., Parikh, V., and Howe, W. M. (2009). Phasic acetylcholine release and the volume transmission hypothesis: time to move on. Nat. Rev. Neurosci. *10*,383–390.

Saunders, A., Granger, A. J. and Sabatini, B. L. (2015). Corelease of acetylcholine and GABA from cholinergic forebrain neurons. eLife. *4.*

Schmiedeberg, O., and Koppe, R. (1869). *Das Muscarin. Das Giftige Alkaloid des Fliegenpilze*s. Leipzig: Vogel.

Schubert, D., Staiger, J. F., Cho, N., Kotter, R., Zilles, K., and Luhmann, H. J. (2001). Layer-specific intracolumnar and transcolumnar functional connectivity of layer V pyramidal cells in rat barrel cortex. J. Neurosci. *21*, 3580–3592.

Schwab, B. C., Kase, D., Zimnik, A., Rosenbaum, R., Rubin, J. E., and Turner, R. S. (2019). Weak modulation of thalamic discharge by basal ganglia output in association with a reaching task. bioRxiv.

Segev, I., and London, M. (2000). Untangling dendrites with quantitative models. Science. *290*, 744–750.

Sethuramanujam, S. et al. (2016). A central role for mixed acetylcholine/GABA transmission in direction coding in the retina. Neuron. *90*, 1243–1256.

Shabel, S. J., Proulx, C. D., Piriz, J. and Malinow, R. (2014). GABA/glutamate co-release controls habenula output and is modified by antidepressant treatment. Science. *345*, 1494–1498.

Shepherd, G. M., Pologruto, T. A., and Svoboda, K. (2003). Circuit analysis of experience-dependent plasticity in the developing rat barrel cortex. Neuron. *38*, 277–289.

Shepherd, G. M., and Svoboda, K. (2005). Laminar and columnar organization of ascending excitatory projections to layer 2/3pyramidal neurons in rat barrel cortex. J. Neurosci. *25*, 5670–5679.

Skydsgaard, M., and Hounsgaard, J. (1994). Spatial integration of local transmitter responses in motoneurones of the turtle spinal cord in vitro. J. Physiol. *479*, 233–246.

Seutin V., Massotte, L., Renette, M. F., and Dresse, A. (2001). Evidence for a modulatory role of I_h on the firing of a subgroup of midbrain dopamine neurons. NeuroReport. *12*, 255–258.

Sossin, W. S., Sweet-Cordero, A., and Scheller, R. H. (1990). Dale's hypothesis revisited: different neuropeptides derived from a common prohormone are targeted to different processes. Proc. Natl. Acad. Sci. USA *87*, 4845–4848.

Spruston, N. (2009). Dendritic signal integration. Northwestern University, Elsevier Ltd.

Steg, G. and Johnels, B. (1994). Physiological mechanisms and movement analysis in Parkinson's disease. Mol. Neurobiol. *9,* 143–147.

Stuart, G., Schiller, J., and Sakmann, B. (1997). Action potential initiation and propagation in rat neocortical pyramidal neurons. J. Physiol. *505*, 617-632.

Stuart, G., and Spruston, N. (1998). Determinants of voltage attenuation in neocortical pyramidal neuron dendrites. J. Neurosci. *18*, 3501–3510.

Stuart, G., Spruston, N., and Hausser, M. (2016). Dendrites. 3rd ed. (Oxford Univ. Press).

Sulzer, D., and Rayport, S. (2000). Dale's principle and glutamate corelease from ventral midbrain dopamine neurons. Amino Acids. *19*, 45–52.

Surmeier, D. J., Ding, J., Day, M., Wang, Z., and Shen, W. (2007). D1 and D2 dopamine-receptor modulation of striatal glutamatergic signaling in striatal medium spiny neurons. Trends Neurosci. *30*, 228–235.

Svensson, E. et al. (2019). General principles of neuronal co-transmission: Insights from multiple model systems. Front. Neural Circuits *12*, 117.

Takács, V.T., Cserép, C., Schlingloff, D., Pósfai, B., Szönyi, A., Sos, K. E., Környei, Z., Dénes, Á., Gulyás, A. I., Freund, T. F., and Nyiri, G. (2018). Co-transmission of acetylcholine and GABA regulates hippocampal states. Nat. Commun. *9*, 2848.

Takakusaki K., Shiroyama T., Yamamoto T., and Kitai S.T. (1996). Cholinergic and noncholinergic tegmental pedunculopontine projection neurons in rats revealed by intracellular labeling. J Comp Neurol. *371*, 345–361.

Talbot, M. J., and Sayer, R. J. (1996). Intracellular QX-314 inhibits calcium currents in hippocampal CA1 pyramidal neurons. J. Neurophysiol. *76*, 2120–2124.

Tong, Q., Ye, C. P., Jones, J. E., Elmquist, J. K., and Lowell, B. B. (2008). Synaptic release of GABA by AgRP neurons is required for normal regulation of energy balance. Nat. Neurosci. *11*, 998–1000.

Tritsch, N. X., Ding, J. B., Sabatini, B. L. (2012). Dopaminergic neurons inhibit striatal output through non-canonical release of GABA. Nature *490*, 262-266.

Tritsch, N. X., Oh, W.-J., Gu, C., Sabatini, B. L. (2014). Midbrain dopamine neurons sustain inhibitory transmission using plasma membrane uptake of GABA, not synthesis. eLife. *3*.

Tritto, T., McCallum, S. E., Waddle, S. A., Hutton, S. R., Paylor, R., Collins, A. C., and Marks, M. J. (2004). Null mutant analysis of responses to nicotine: Deletion of β2 nicotinic acetylcholine receptor subunit but not α7 subunit reduces sensitivity to nicotine-induced locomotor depression and hypothermia. Nicotine & Tobacco Research. *6*, P145–157.

Turrini, P., Casu, M. A., Wong, T. P., De Koninck, Y., Ribeiro-da-Silva, A., and Cuello, A. C. (2001). Cholinergic nerve terminals establish classical synapses in the rat cerebral cortex: synaptic pattern and age-related atrophy. Neuroscience. *105*, 277–285.

Umbriaco, D., Watkins, K. C., Descarries, L., Cozzari, C., and Hartman, B. K. (1994). Ultrastructural and morphometric features of the acetylcholine innervation in adult rat parietal cortex: an electron microscopic study in serial sections. J. Comp. Neurol. *348*, 351–373.

Urban, N. N., and Barrionuevo, G. (1998). Active summation of excitatory postsynaptic potentials in hippocampal CA4 pyramidal neurons. Proc. Natl. Acad. Sci. *95*, 11450–11455.

Vetter, P., Roth, A., and Häusser, M. (2001). Propagation of action potential in dendrites depends on dendritic morphology. J. Neurophys. *85*, 926–37.

Wang, H., et al. (2007). High-speed mapping of synaptic connectivity using photostimulation in Channelrhodopsin-2 transgenic mice. Proc. Natl. Acad. Sci. USA. *104*, 8143–8148.

Watabe-Uchida, M., Zhu, L., Ogawa, S. K., Vamanrao, A., and Uchida, N. (2012). Whole-brain mapping of direct inputs to midbrain dopamine neurons. Neuron. *74*, 858–873.

White, E. L. (2002). Specificity of cortical synaptic connectivity: emphasis on perspectives gained from quantitative electron microscopy. J. Neurocytol. *31*, 195–202.

Whiting P., and Lindstrom J. (1986). Pharmacological receptors properties of immuno-isolated neuronal nicotinic. J. Neurosci. *6*, 3061–3069.

Whiting I. P. J., Swanson L.W., and Simmons D. M. (1987). lmmunohistochemical localization of neuronal nicotinic receptors in the rodent central nervous system. J. Neurosci. *7*, 3334–3342.

Williams, S. R., and Stuart, G. J. (2002). Dependence of EPSP efficacy on synapse location in neocortical pyramidal neurons. Science. *295*, 1907–1910.

Williams, S. R., and Stuart, G. J. (2003). Role of dendritic synapse location in the control of action potential output. Trends Neurosci. *26*, 147–154.

Wilson, C. J., Groves, P. M., and Fifkovà, E. (1977). Monoaminergic synapses, including dendro-dendritic synapses in the rat substantia nigra. Exp. Brain Res. *30*,161–74.

Wise, R.A. (2009). Roles for nigrostriatal–not just mesocorticolimbic–dopamine in reward and addiction. Trends Neurosci. *32*, 517–524.

Wong, R. K., and Prince, D. A. (1978). Participation of calcium spikes during intrinsic burst firing in hippocampal neurons. Brain Res. *159*, 385–390.

Wong, R. K., Prince, D. A., and Basbaum, A. I. (1979). Intradendritic recordings from hippocampal neurons. Proc. Natl. Acad. Sci. *76*, 986–990.

Wyckoff, R. W. G., and Young, J. Z. (1956). The motorneuron surface. Proc. Roy. Soc. *144*, 440-50.

Xiao, C., Nashmi, R., McKinney, S., Cai, H., McIntosh, J. M., and Lester, H. A. (2009). Chronic nicotine selectively enhances a4b2* nicotinic acetylcholine receptors in the nigrostriatal dopamine pathway. J. Neurosci. *29*, 12428–12439.

Xiao, C., Cho, J. R., Zhou, C., Treweek, J. B., Chan, K., McKinney, S. L., Yang, B., and Gradinaru, V. (2016). Cholinergic mesopontine signals govern locomotion and reward through dissociable midbrain pathways. Neuron. *90*, 333–347.

Yohrling, G., Jiang G. C., DeJohn, M. M., Miller, D. W., Young, A. B., Vrana, K. E., and Cha, J. H. (2003). Analysis of cellular, transgenic and human models of Huntington's disease reveals tyrosine hydroxylase alterations and substantia nigra neuropathology. Brain Res *119*, 28–36.

Yuste, R., Gutnick, M. J., Saar, D., Delaney, K. R., and Tank D. W. (1994). Ca2+ accumulations in dendrites of neocortical pyramidal neurons: an apical band and evidence for two functional compartments. Neuron. *13*, 23–43.

Zecca, L., Zucca, F. A., Wilms, H., and Sulzer, D. (2003). Neuromelanin of the substantia nigra: a neuronal black hole with protective and toxic characteristics. Trends Neurosci. *26*, 578–580.

Zhang, L., Weiner, J. L., Valiante, T. A., Velumian, A. A., Watson, P. L., Jahromi, S. S., Schertzer S., Pennefather, P., and Carlen, P. L. (1994). Whole-cell recording of the Ca2+-dependent slow afterhyperpolarization in hippocampal neurones: effects of internally applied anions. Pflugers Arch *426*, 247– 253.